The experimental and numerical investigation of fracture behaviour in PMMA notched specimens under biaxial loading conditions – Tension with torsion

Elżbieta Bura [a,*], Wojciech Grodzki [a], Andrzej Seweryn [b]

[a] *Faculty of Mechanical Engineering, Bialystok University of Technology, Poland*
[b] *Faculty of Mechanical Engineering and Ship Technology, Gdansk University of Technology, Poland*

ABSTRACT

This paper presents the results of experimental fracture test of flat PMMA specimens under biaxial loading condition tension with torsion (proportional). The specimens were made in two thicknesses: 5 and 15 mm and were weakened with V-type edge notches with different root radii: 0.5; 2 and 10 mm. Thanks to the ARAMIS 3D 4 M non-contact vision system, measurement of the elongation and twist angle were recorded. During experimental part all of the deformation processes were observed using PHANTOM cameras. Obtained records made it possible to precisely indicate the moment of crack initiation (tensile force and torsional moment values). Using the microscopic observations the location of crack initiations were determined. Results obtained for biaxial loading were compared with those obtained for uniaxial tension and torsion. Based on experimental data the numerical calculation with FEM were carried out. The principal stress and plastic strain distribution under critical load, were obtained. The points of occurrence of stress maxima and plastic strain were indicated, which were taken as potential crack initiation sites. On the basis of the stress and plastic strain values measured at the critical points, a stress–strain fracture criterion was formulated, which was then positively verified. Additionally, new form of stress–strain fracture criterion was proposed. The bilinear form of the fracture criterion can be successfully used to predict fracture in PMMA flat specimens, regardless of the notch root radius, type of load or element thickness.

1. Introduction

By far the most common experimental and numerical studies of the fracture of notched elements made of Polymethylmethacrylate (PMMA) concern simple loading conditions and pure crack/notch failure types. The fracture of this type of component during mode I has been described in a number of works in tension [1,2,3,4,5,6,7,8] also in compression [1,9,10,11,12,13,14]. Similarly, PMMA fracture during mode III in twisted components has been the subject of several scientific publications [15,16,17]. Under real operating conditions, these components most often experience fracture in mixed modes, which determines the current focus of research in works on fracture mechanics. Components made from plastics can be found in many industries: architecture, furniture, transport, electronics, but above all in medicine. Polymethylmethacrylate (PMMA) is used, for example, as a glass substitute in construction and architecture.

---

* Corresponding author.
E-mail addresses: e.bura@pb.edu.pl (E. Bura), w.grodzki@pb.edu.pl (W. Grodzki), andrzej.seweryn@pg.edu.pl (A. Seweryn).

Nomenclature

|	
g	specimen thickness
E	Young's modulus
n	the vector normal to the physical plane
$R_{0.2}$	yield stress
$R_{0.05}$	elastic limit
$\dot{u}$	linear displacement velocity
x_0	the vector defining the location of crack initiation
$\dot{\phi}$	torsion angle increment of the specimen base
F^I	critical tensile force obtained in pure tension tests
M_s^{III}	critical torsional moment obtained in pure torsion tests
$F^{I/III}$	critical tensile force obtained in biaxial test
$M_s^{I/III}$	critical torsional moment obtained in in biaxial test
ε_1^p	maximum principal plastic strain
ε_c	critical value of plastic strain
ε_{max}^p	maximum value of plastic strain
ε_{gr}	limit deformation used in the stress–strain fracture criterion
σ_1	maximum principal stress
σ_{max}	maximum value of stress
σ_n	the normal stress on the physical plane
σ_c	the failure stress in the damaged material
σ_{c0}	the failure stress in the undamaged material
ω	damage state variable.
ρ	notch root radius
ν	Poisson's ratio
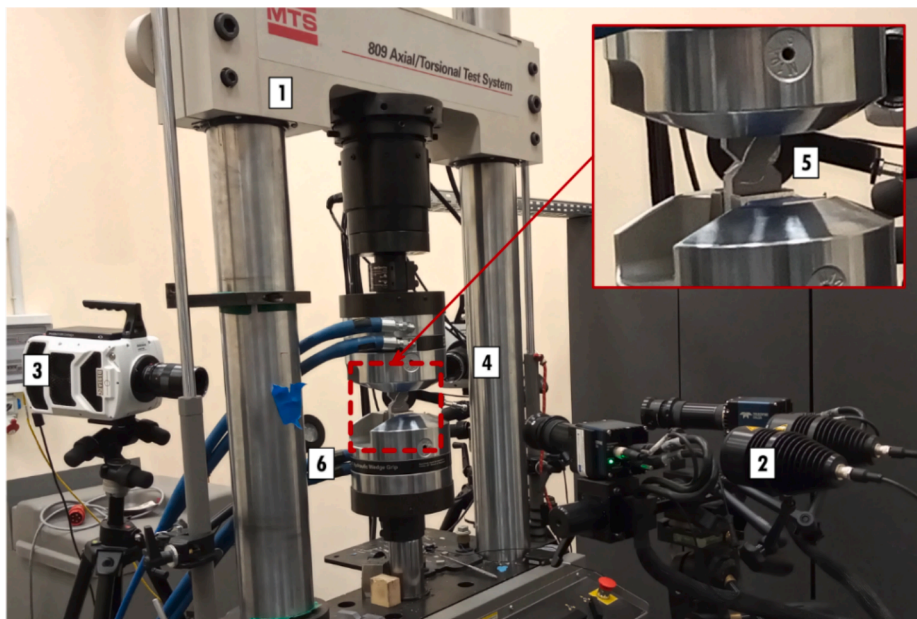
Fig. 1. Test stand: 1 – MTS 809.10 testing machine, 2 – ARAMIS 3D 4 M vision system, 3 – PHANTOM v1610 camera, 4 – PHANTOM v2011 camera, 5 – specimen, 6 – LED lights.

Its high impact strength and weather resistance have also made PMMA widely used in the automotive industry, e.g. in caravan windows, covers on motorbikes, aircraft, helicopters. The transparency of this material makes it ideal for optical and lighting applications. It can also be found in electronics, such as LCD monitors. It is also found in medical applications due to the biocompatibility and biodegradability of this material. A wide group of works deals with the fracture of plastics (mainly PMMA) during mixed-mode I +

Table 1

Test parameters: tensile with torsion.

Nominal notch root radius	Nominal specimen thickness	$\dot{u}$	$\dot{\phi}$
[mm]	[mm]	[mm/s]	[°/s]
0.5	5	0.04	2.85
0.5	15		0.88
2	5	0.04	1.65
2	15		0.68
10	5	0.04	1.00
10	15		0.40

Table 2

Critical values of tensile force, torsional moment, base elongation and twist angle for notched specimens subjected to biaxial loading.

Specimen	Actual specimen thickness [mm] ± 0.01	Maximum twist angle [°]		Critical torsional moment value** [Nm]		Maximum elongation [mm]		Critical tensile force value* [kN]	
			average		average		average		average
RS 05–1-5	4.90	5.82		5.44		0.07		1.24	
RS 05-2-5	4.90	6.10	**6.08**	5.84	**5.68**	0.07	**0.07**	1.22	**1.25**
RS 05-3-5	4.92	6.31		5.77		0.08		1.29	
RS 05-1-15	14.43	2.96		41.63		0.09		4.11	
RS 05-2-15	14.64	2.60	**2.76**	39.07	**39.58**	0.09	**0.09**	3.76	**3.88**
RS 05-3-15	14.55	2.71		38.03		0.09		3.77	
RS 2-1-5	4.95	9.50		8.29		0.19		2.86	
RS 2-2-5	4.93	8.30	**9.08**	8.26	**8.17**	0.17	**0.19**	2.82	**2.82**
RS 2-3-5	4.92	9.45		7.95		0.20		2.79	
RS 2-1-15	14.07	4.41		52.20		0.18		7.08	
RS 2-2-15	14.04	4.21	**4.36**	49.34	**51.29**	0.17	**0.18**	6.65	**6.90**
RS 2-3-15	14.08	4.45		52.33		0.18		6.97	
RS 10-1-5	4.92	13.19		9.43		0.43		5.23	
RS 10-2-5	4.94	19.94	**17.89**	11.57	**10.92**	0.65	**0.59**	6.40	**6.03**
RS 10-3-5	4.92	20.54		11.75		0.68		6.45	
RS 10-1-15	14.27	14.01		59.25		0.96		18.09	
RS 10-2-15	14.31	13.46	**14.62**	60.79	**58.95**	0.93	**1.02**	18.25	**18.29**
RS 10-3-15	14.19	16.40		56.80		1.17		18.53	

*Percent error of tensile force: ≤ 1.999kN – 0.06 %; ≤ 4.001kN – 0.06 %; ≤ 8.007kN – 0.08 %; ≤ 10.009kN – 0.09 %; ≤ 20.024kN – 0.12 %;
**Percent error of torque: ≤ 20Nm – 0.10 %; ≤ 40Nm – 0.12 %; ≤ 60 Nm – 0.15 %.

Table 3

Critical values of tensile force and torsional moment for specimens with notches subjected to biaxial loading.

ρ	g	Critical torsional moment value** [Nm]		$m = \dfrac{M_s^{I+III}}{M_s^{III}}$	Critical tensile force value* [kN]		$f = \dfrac{F^{I+III}}{F^I}$	$\dfrac{m}{f}$
[mm]	[mm]	III	I/III		I	I/III		
0.5	5	13.92	5.68	**0.41**	2.74	1.25	**0.46**	**0.89**
	15	76.88	39.38	**0.51**	8.88	3.88	**0.44**	**1.16**
2	5	12.92	8.17	**0.63**	4.55	2.83	**0.62**	**1.02**
	15	81.76	51.29	**0.63**	12.94	6.90	**0.53**	**1.18**
10	5	14.38	10.92	**0.76**	7.88	6.03	**0.76**	**1.00**
	15	84.70	58.95	**0.70**	23.05	18.29	**0.79**	**0.89**

*Percent error of tensile force: ≤ 1.999kN – 0.06 %; ≤ 4.001kN – 0.06 %; ≤ 8.007kN – 0.08 %; ≤ 10.009kN – 0.09 %; ≤ 20.024kN – 0.12 %;
**Percent error of torque: ≤ 20Nm – 0.10 %; ≤ 40Nm – 0.12 %; ≤ 60 Nm – 0.15 %.

II. Bahrami et al. [18] studied experimentally and theoretically fracture in PMMA SENB-type components. The moment of crack development was predicted using the theory of critical distance (TCD) together with the generalised strain energy density criterion (GSED). The approach adopted was that a crack propagates when the strain energy reaches its critical value at a certain critical distance. A better performance of the GSED criterion, compared to the classical strain energy density criterion (SED), was established in predicting the fracture of notched components made of PMMA.

Notched PMMA SCB (semi-circular bend) specimens were subjected to three-point bending [19]. The fracture of the components was analysed for pure mode I, mode II and mixed-modes I + II. It was shown that the traditional maximum tangential stress criterion (MTS) criterion does not allow the prediction of the critical load value and the direction of crack growth with reasonable accuracy. A generalised MTS criterion was therefore applied, taking into account the effect of T-stress. Crack propagation was simulated using the
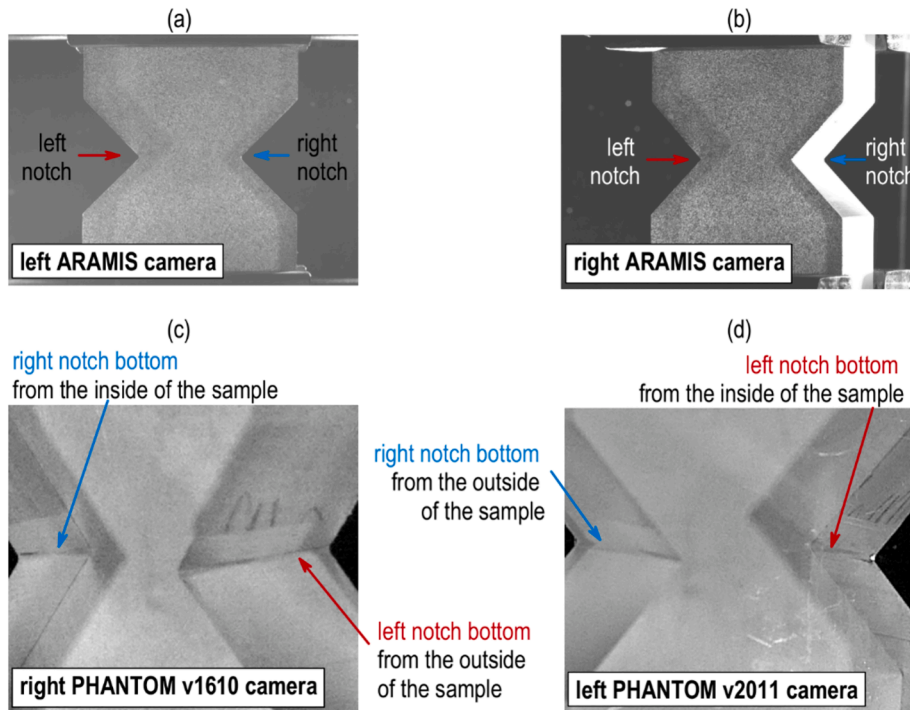
Fig. 2. View from cameras used in the study: a-b) ARAMIS cameras, c) PHANTOM v1610 camera and d) PHANTOM v2011 camera.

finite element method. It was shown that the adopted technique provides a very good estimate of the crack growth path in PMMA tests if the crack growth direction is determined by the generalised MTS criterion. PMMA components of the Brazilian disc (CCBD) and asymmetric semi-circular bending (AASCB) types were subjected to compression tests in the work of Bahrami et al. [20]. In the considerations described, the focus was on taking into account the frictional forces occurring during compression and their influence on the accuracy of the prediction of the fracture process. A procedure was developed using the concept of the MTS criterion supplemented by the results of finite element method (FEM) calculations, and critical load values corresponding to the crack initiation moment during compression were obtained. The simplicity and effectiveness of the described method was demonstrated, and it was pointed out that neglecting the effect of frictional forces during fracture analysis for the compression case can result in an underestimation of the critical load by up to 60 %. Brazilian disc type specimens were also used in their study by Ayatollahi and Aliha [21]. PMMA components weakened by a central diamond-shaped notch were subjected to compression tests, thus mode I, mode II and mixed-mode I + II fracture was realised (depending on the angle of the notch formation with respect to the loading axis). The MTS criterion was extended to the case studied by formulating the RV-MTS criterion. Good agreement was shown between theoretical predictions and experimental results for both mixed-mode fracture toughness and fracture initiation angle. The authors have followed up similar work [22].

A paper by Aliha et al. [23] investigated the effect of loading speed (from 1 to 200 mm/min) on the fracture process in specimens made from notched-beam PMMA − short bend beam (SBB) type. The study analysed fracture in modes I, II and mixed-modes I + II. In order to predict the fracture process, the GMTS criterion was used, which allowed the critical load values to be close to the experimental data. Similar considerations have also been described in other works [24,25]. Foti et al. [26] analysed the fracture of flat specimens (thickness equal to 3 mm) made of PMMA, weakened on both sides with U-notches. Tensile tests were conducted at a speed of 2 mm/min. By using different angles of inclination of the symmetry axis of the notches with respect to the main axis of the specimen, the components were subjected to both mode I, II and mixed-mode I + II fracture. Different notch root radii were also used. Using the SED criterion and TCD theory, high agreement between numerical predictions and experimental data was obtained. The use of the digital gradient sensor (DGS) method to directly investigate the notch-bottom deformation of notch-weakened PMMA specimens is described in the work of Zhang et al. [27]. In this study, the values of stress intensity factors were determined for pure I, II and mixed-modes I + II, and the results were compared with data obtained by numerical FEM calculations. The effectiveness and practicality of the DGS method for measuring stress intensity factors (SIF) was confirmed. Using ABS fibres by 3D printing, U-notched diagonally loaded square plate (UNDLSP) specimens were fabricated and subsequently subjected to mixed-mode I + II [28]. The virtual isotropic material concept (VIMC) was used to predict fracture in the cases studied, together with two well-known brittle models MTS and MS. The paper confirms that both the VIMC-UMTS and VIMC-UMS criteria accurately predict the critical load values experimentally. Ayatollahi and Aliha [29] described an experimental study of PMMA cracking during tensile fracture of a square plate-shaped specimen centrally weakened by a diagonal notch (DLSP). Fracture during mixed-mode I/II was analysed. Based on the experimental data obtained, the effectiveness of fracture prediction using the MTS criterion was positively verified. Ayatollahi and Torabi [30] proposed
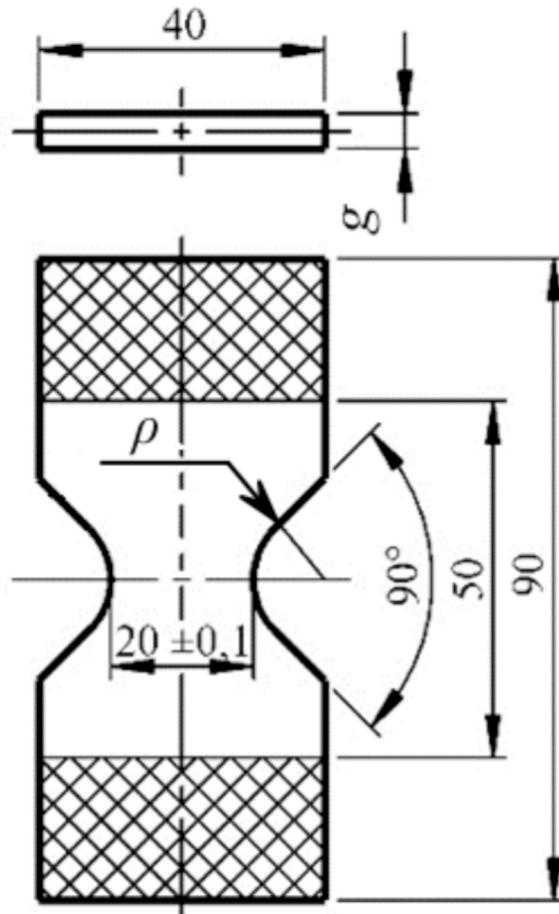
Fig. 3. Notched specimens: $\rho = 0.5$, 2, and 10 mm; $g = 5$ and 15 mm.

the UMTS criterion for predicting the brittle fracture of U-notched elements under static loading during mixed-mode I + II. Based on the three-point bending tests carried out, it was shown that there is a good agreement between the results of the UMTS criterion and the experimental data.

Bidadi et al. [31] proposed a maximum tangential strain criterion for predicting fracture during mixed-mode I + III. Based on this criterion, the out-of-plane crack initiation angle and fracture toughness were theoretically predicted under I + III mixed-mode loading conditions. The results showed that the T-stress has no effect on the out-of-plane crack initiation angle. In this study, this criterion was verified for various brittle and quasi-brittle materials during mixed-mode I + III, such as specimens of the edge notch disc bend (ENDB) [32], rectangular beam with an inclined crack (ISENB) [33] and the semi-circular bend (SCB) [34]. The predicted results were consistent with the data obtained in the experiments. Shen et al. [35] confirmed the effectiveness of the modified 3D G-criterion for predicting fracture under mixed-mode I + III. Experimental and theoretical values of: inclination angle, torsion angle and critical stress intensity factors (SIF) for PMMA and GPPS were compared. Axially-symmetric ring-notched specimens were fabricated from PMMA and also from 7050 aluminium alloy, and then subjected to tensile tests with torsion [36]. The prediction of fracture processes was based on the determination of the maximum normal stress and the maximum shear stress on an inclined plane at the same distance from the crack face. The ratio of these two types of stress was compared with the fracture toughness of the material. It was found that under proportional loading conditions, the ratio of these stress components can maintain almost the entire elastic range up to fully plastic, which can contribute to effective predictions of fracture processes. Similar aluminium alloy specimens were also subjected to tensile-torsion fracture tests, the results of which are described in [37]. A new general criterion for mixed-mode fracture based on the concept of maximum potential energy release rate (MPERR) is presented. This criterion can be easily transformed to a pure mode fracture criterion and can also be reduced to the commonly accepted mixed-mode fracture criteria I + II. The experimental results are consistent with the predictions of the proposed criterion. Susmel and Taylor studied PMMA specimens under tension with torsion [38]. Different fracture mechanisms were established depending on the contribution of each type of loading. The prediction of the moment of crack initiation was done using the extended TCD concept, allowing predictions to be made within an error range of approximately ± 20 %. Ayatollahi and Saboori [39] proposed a new approach to study fracture in PMMA during mixed-mode I + II. They described the concept of the device that was used in the experimental studies. The results of numerical calculations determined the device
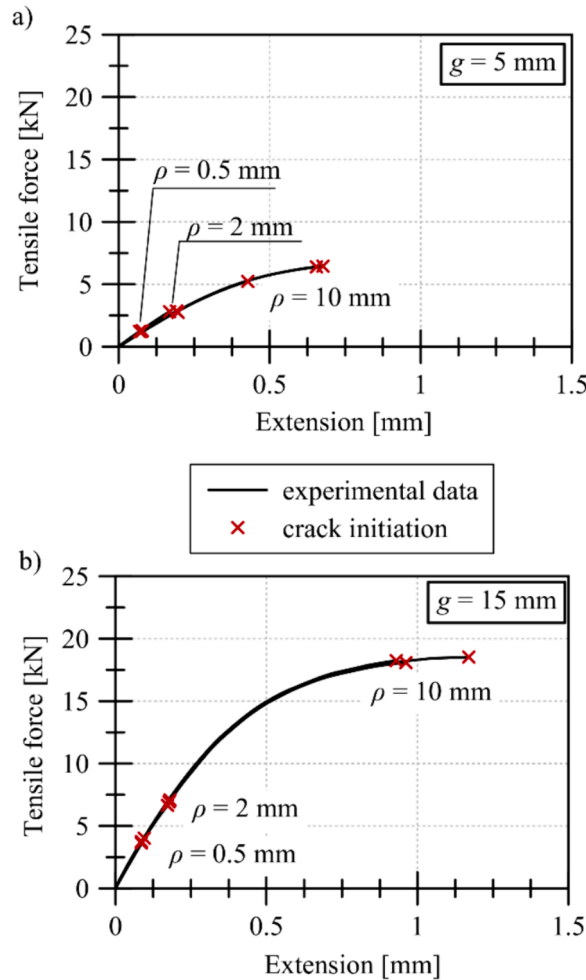
Fig. 4. Tensile curves for specimens with notch root radius equal to $\rho = 10$, 2 and 0.5 mm, with nominal thickness (a) $g = 5$ mm, (b) $g = 15$ mm.

configurations and corresponding loading conditions. The experimental critical load values and fracture angles were determined relatively accurately based on the maximum tangential stress criterion (MTS). The discussed stand was also used by Saboori et al. [40]. They conducted a series of fracture experiments on U-notch weakened PMMA specimens on it. Two brittle fracture criteria were verified, i.e.: the point stress (PS) criterion and the mean stress (MS) criterion. It was found that in the studied cases both criteria are accurate enough to predict the fracture process. It was indicated that the angle of out-of-plane fracture caused by pure mode III is constant and independent of the notch root radius. Flat pieces with keyhole-shaped notches were made of PMMA and subjected to tension with shear [41]. Samples were prepared with three different notch root radii to evaluate the effect of its on fracture toughness. Notch stress intensity factors (NSIF) were determined based on the maximum tangential stress (MTS) and mean stress (MS) criteria. It was shown that for all notch root radii, the results obtained for the MTS and MS criteria are consistent with experimental data. Sysmel and Taylor [38] developed a test apparatus study the fracture behaviour of PMMA notched flat specimen subjected to tensile and shear loads (Mode I and II) and circumferentially notched bar specimen subjected to combined tensile and torsional loading (Mode I and III). It has been shown that the fracture behaviour for superimposed modes I and III indicates a strong influence of non-linear deformation, which causes the mixed-mode strength to depend on the order and type of loading.

The SED criterion [42] has been used to predict fracture in specimens made of PMMA weakened with notches given mixed-mode I + II [43]. The authors verified the usefulness of this criterion on the basis of independently conducted fracture tests, but also on data collected in the literature, paying particular attention to the different values of the mixed-mode ratio. It was shown that there is good agreement between theoretical estimates and experimental data.

Currently, PMMA material is the subject of many studies on fracture. The most recent considerations are related to the study of the phenomenon of fracture under biaxial loading conditions, which is due to the real operating conditions of components made of plastic. The main objective of the research described in the literature is to learn about the fracture phenomenon of these materials, including, first of all, the determination of critical load values and also the location and angle of crack initiation. Another important step is to establish a relationship that will allow to predict this process and thus prevent its negative consequences. Among the most popular
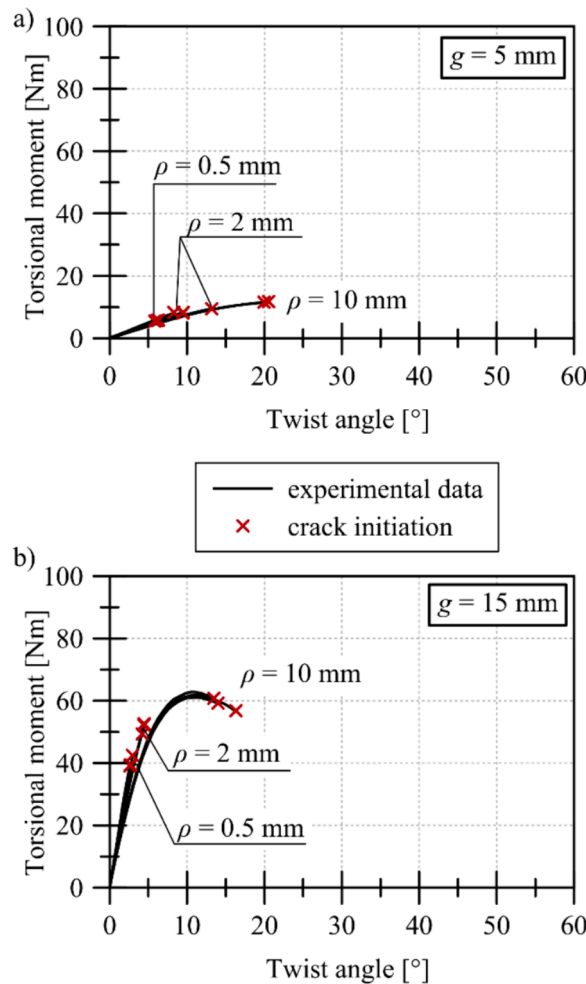
Fig. 5. Torsional curves for specimens with notch root radius equal to $\rho = 10$, 2 and 0.5 mm, with nominal thickness (a) $g = 5$ mm, (b) $g = 15$ mm.

criteria in the context of PMMA fracture appear the classic brittle fracture criteria, i.e. PS, MTS or MS, which allow to accurately predict, for example, the value of the critical load, when the nature of the tested material is typically brittle or quasi-brittle. In the literature, there is a lack of fracture tests in the mixed-mode I + III on flat specimens directly loaded with torsional moment and tensile force. Results of such studies are available, but for tensile tests carried out using additional equipment. Also, no fracture tests of PMMA taking into account the thickness effect were found, as mostly thin specimens were tested by maintaining plain stress state. In addition, most of the PMMA fracture test procedures described in the literature were carried out at relatively high strain rates; in the present study, a relatively low value of the averaged strain rate was used, which forces a pronounced plasticisation of the test material, especially during torsion and complex loading states. This article attempts to describe in detail the phenomenon of fracture in PMMA under conditions in which this material is characterized by high nonlinearity and significant influence of plastic strain. Flat elements were weakened with V-notches with different notch root radii and subjected to tension with torsion (proportional loads). The results obtained were compared with those obtained under uniaxial tension and torsion [16,44]. These two papers describe, respectively, experimental testing [16] and numerical modelling [44] of the fracture processes of PMMA notched specimens operating under simple loading conditions. They discuss the results of experimental testing and numerical modelling for the separate cases of (a) uniaxial tension and (b) torsion. In this way, fracture processes during pure notch failure types, i.e. mode I and mode III, were analysed. These investigation was the starting point for conducting fracture studies in the complex loading condition, i.e. mixed-mode I + III, which are described in this manuscript. The tensile-torsion tests required separate tensile and torsion tests to be carried out beforehand, in order to determine the critical load values − these determined later, i.e. in the tensile-torsion tests, the percentage of both types of load.

The results obtained experimentally for mixed-mode I + III, were used for numerical calculations using the finite element method, which made it possible to estimate the values of stress and plastic strain under critical loading conditions. The present considerations allowed the formulation of the stress–strain form of the fracture criterion, which allows the prediction of critical load values with an accuracy that makes it possible to apply the method in engineering practice.
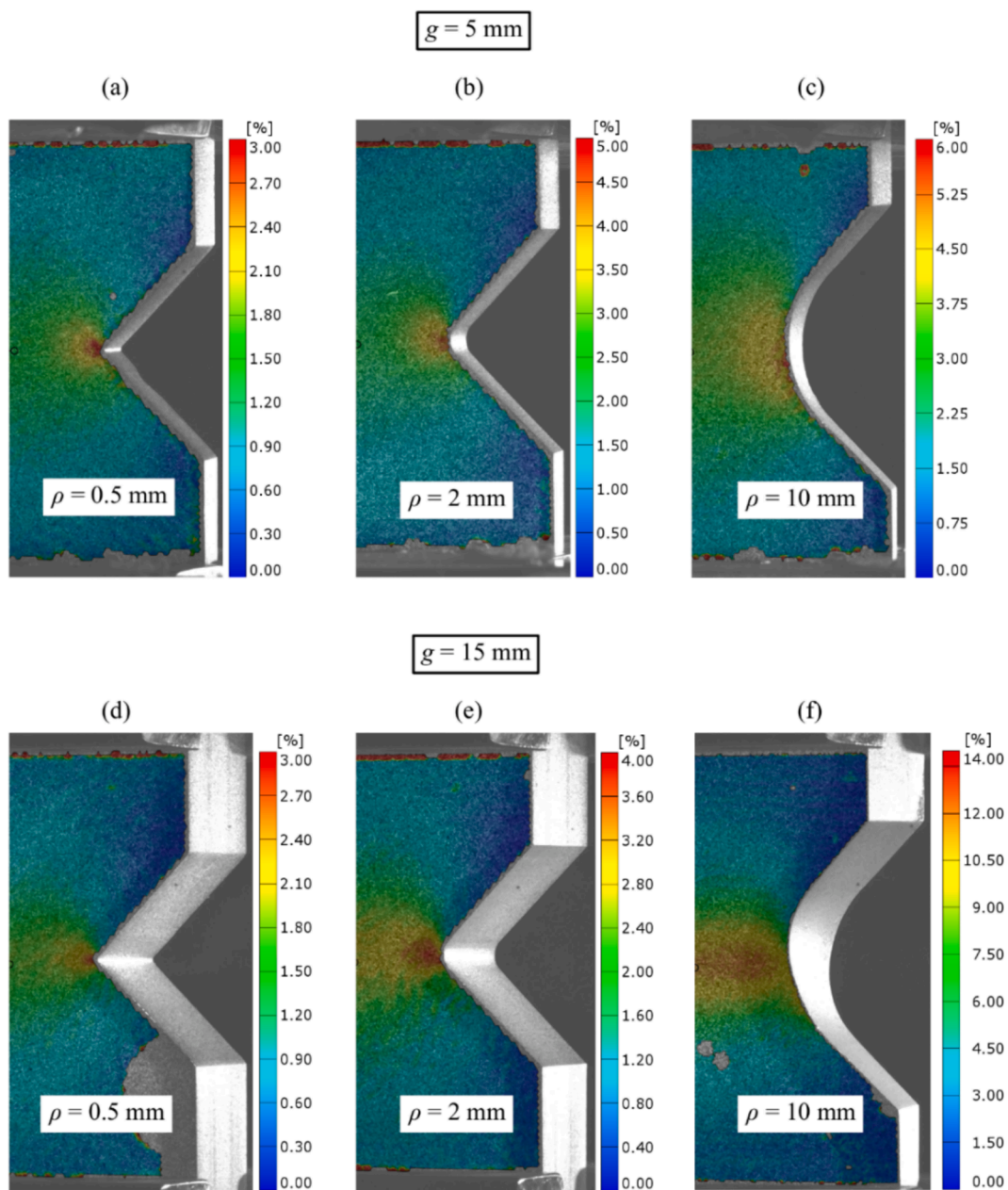
Fig. 6. Distribution of equivalent plastic strain on the front face of the specimen moments before the initiation of rupture. Specimen thickness equal to 5 mm: (a)-(b) and 15 mm (d)-(f).
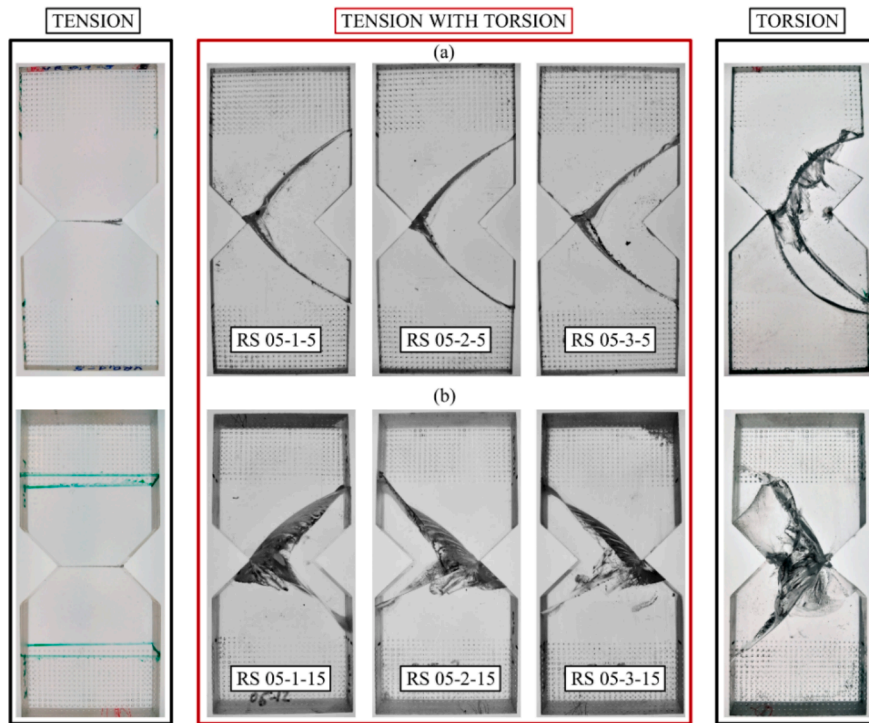
Fig. 7. Specimens with notch root radius $\rho = 0.5$ mm after the biaxial tests: a) $g = 5$ mm and b) $g = 15$ mm.
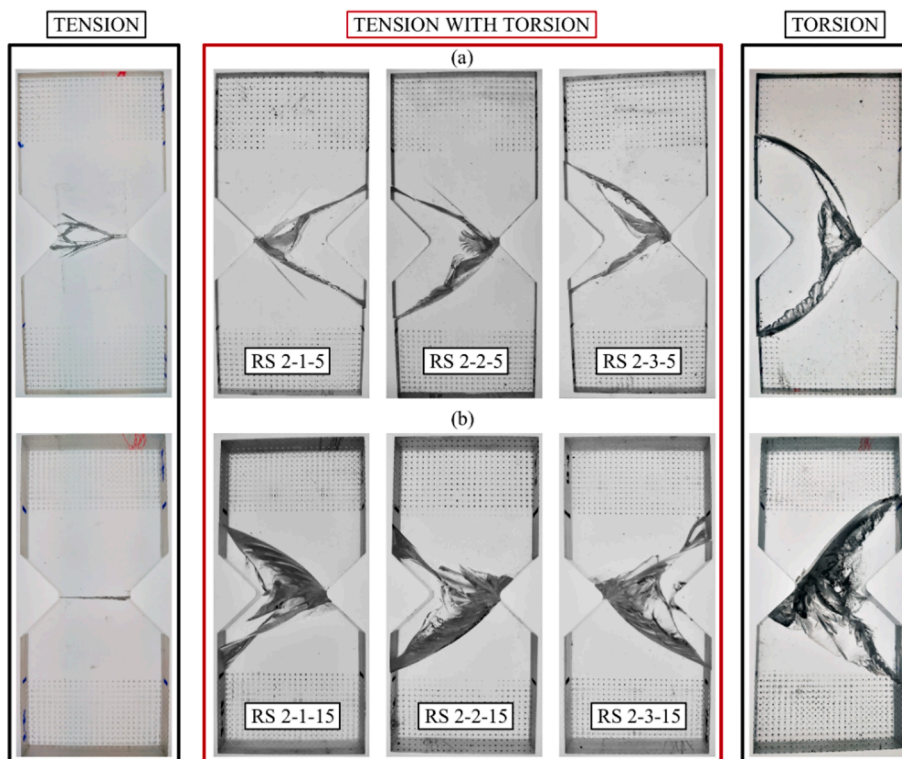

Fig. 8. Specimens with notch root radius $\rho = 2$ mm after the biaxial tests: a) $g = 5$ mm and b) $g = 15$ mm.
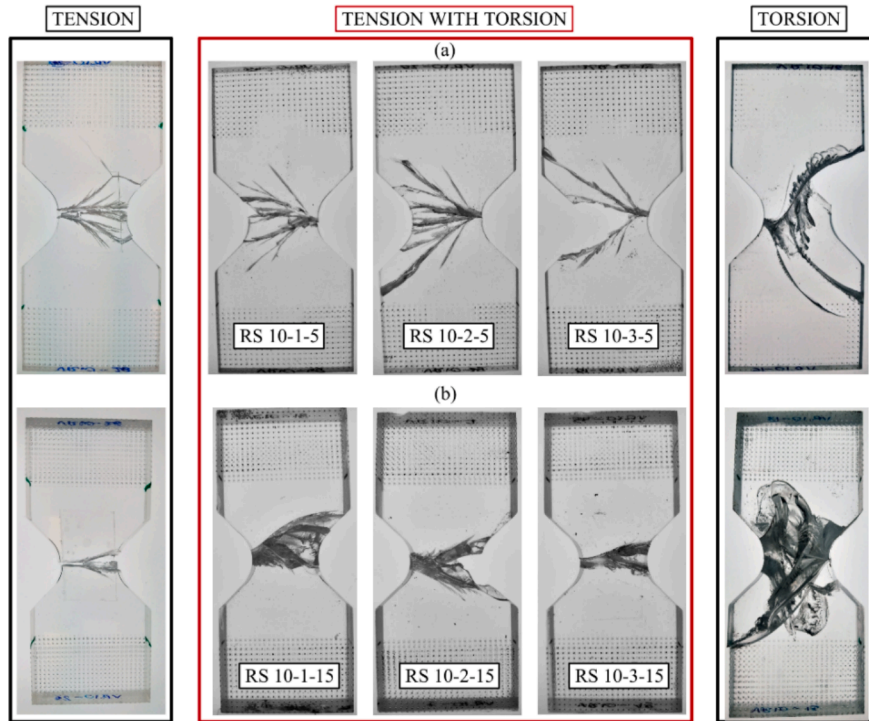
Fig. 9. Specimens with notch root radius $\rho = 10$ mm after the biaxial tests: a) $g = 5$ mm and b) $g = 15$ mm.

2. Testing procedure and results

Test were carried out using an MTS 809.10 dynamic biaxial testing machine (with a measuring range of tensile force: ± 100 kN and torque ± 1100 Nm). The test stand is shown in Fig. 1. The process was recorded using two PHANTOM cameras. The cameras recorded at the following speeds: 220 000 frames/s – Phantom v2011, 160 000 frames/s – Phantom v1610. As the crack initiated once in the left and once in the right notch, each camera observed one of the notches. The Phantom cameras were used in order to more accurately indicate the moment and location of crack initiation. Synchronising the testing machine with the Phantom cameras allowed a more accurate indication of the critical load value (responsible for crack initiation). Without them this would not have been possible; the load–displacement curves do not show significant changes in their trends at the time of crack initiation, which is additionally not visible to the naked eye. Without the use of the cameras, it would be possible to determine that a crack is already at an advanced stage of its development. Two LED lamps were used to illuminate the samples from the side of the lenses.

The torsion angle and elongation of the measuring base was measured by using the ARAMIS 3D 4 M vision system, which is used for non-contact displacement measurements by means of digital image correlation. The recording speed was between 10 and 20 frames per second. The vision system was used in the following settings: camera lens: 100 mm, tilt angle of the cameras: 25 degrees, CP20 calibrator 55 mm x 44 mm, distance from the tested object 685 mm, distance between cameras 274 mm, matrix resolution 2400x1728 pixels, calibration deviation: 0.025 pixel, calibration coefficient: 0.018–0.025 pixel. The system was also synchronised with the testing machine. Using the results obtained from the displacement of the grips of the measuring machine would have generated large errors. The lack of extensometers with the required measuring range necessitated the use of a non-contact measuring system. Both systems were used simultaneously. Each of them was synchronized with the testing machine. The observations with the Phantom cameras did not interfere with the observations with the ARAMIS 3D 4 M vision system, as each of the systems was observed from two different sides.

The experiment was conducted under displacement control. Experimental investigations of fracture under a biaxial loading condition, i.e. tensile with torsion began by determining the linear displacement velocity $\dot{u}$ and torsion angle increment $\dot{\phi}$ of the specimen base (Table 1). The loads were applied proportionally, i.e. the specimen was loaded simultaneously with a tensile force and a torsional moment so that, at a given moment, the specimen experienced a load equal to the same proportion of the critical tensile force obtained in pure tension tests f and the same proportion of the critical torsional moment m obtained in pure torsion tests [16]. A linear displacement velocity of 0.04 mm/s was assumed (on a measuring base of 50 mm − the same conditions as in the pure tensile tests [16]. The angular displacement velocity was then varied so that the ratio of the m/f parameters (Table 3) was as close to unity as possible. The procedure was repeated for each specimen type. The loading velocities were selected to maintain the same average strain rate in all test samples, consequently a single hardening curve could be used for numerical modelling.

In addition, Fig. 2 shows the perspectives from which the sample was observed during the test. In each experiment, two recordings were obtained from the ARAMIS video system cameras (on the side of the painted sample, Fig. 2a,b) and two recordings from the
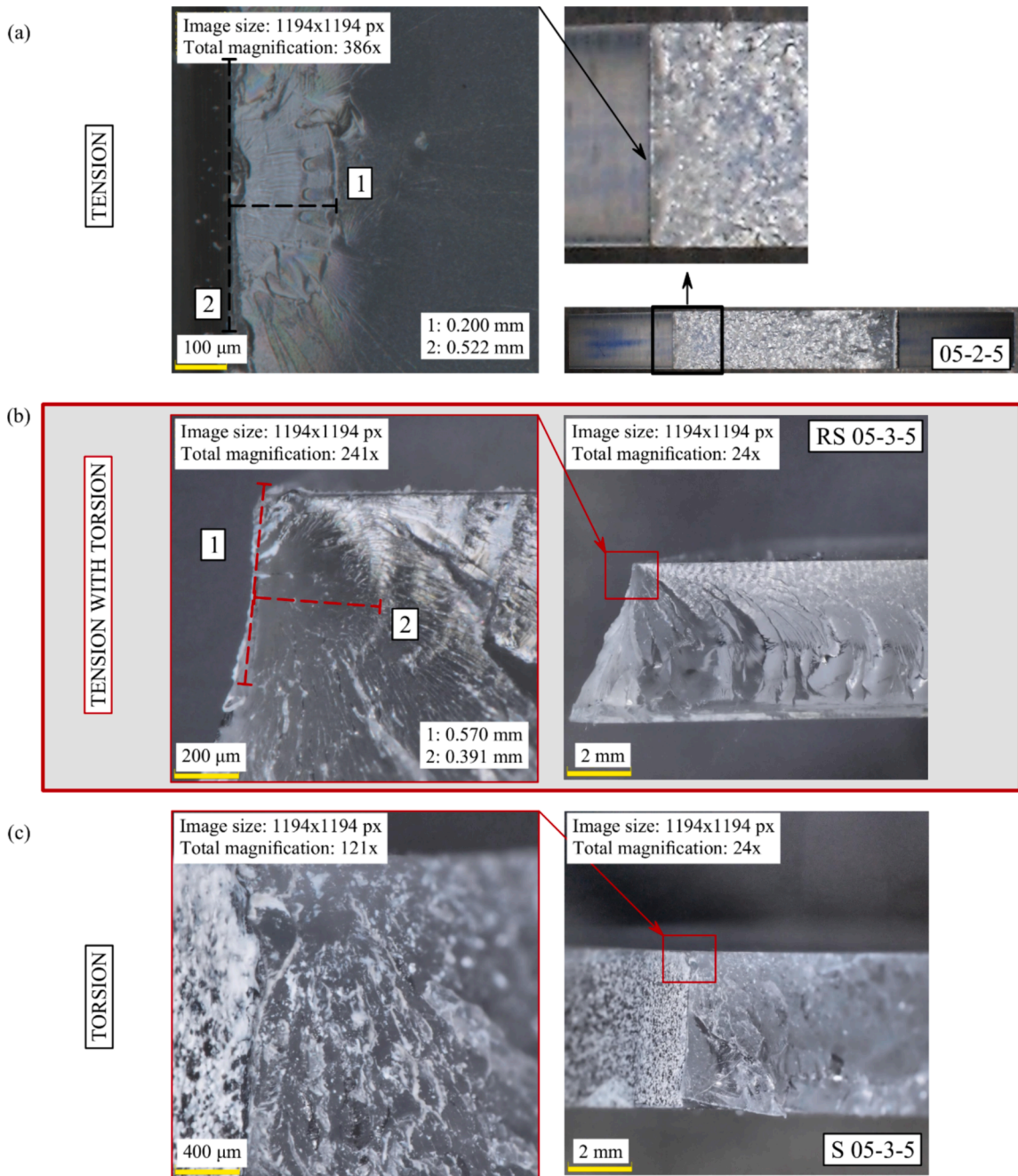
Fig. 10. Microscopic images of fracture surfaces of specimens subjected to: a) tension [16], b) tension with torsion and c) torsion [16], weakened by V-notches with rounding radius ρ = 0.5 mm: places of crack initiation and their characteristic dimensions.

Fig. 11. Microscopic images of fracture surfaces of specimens subjected to: a) tension [16], b) tension with torsion and c) torsion [16], weakened by V-notches with rounding radius ρ = 2 mm: places of crack initiation and their characteristic dimensions.
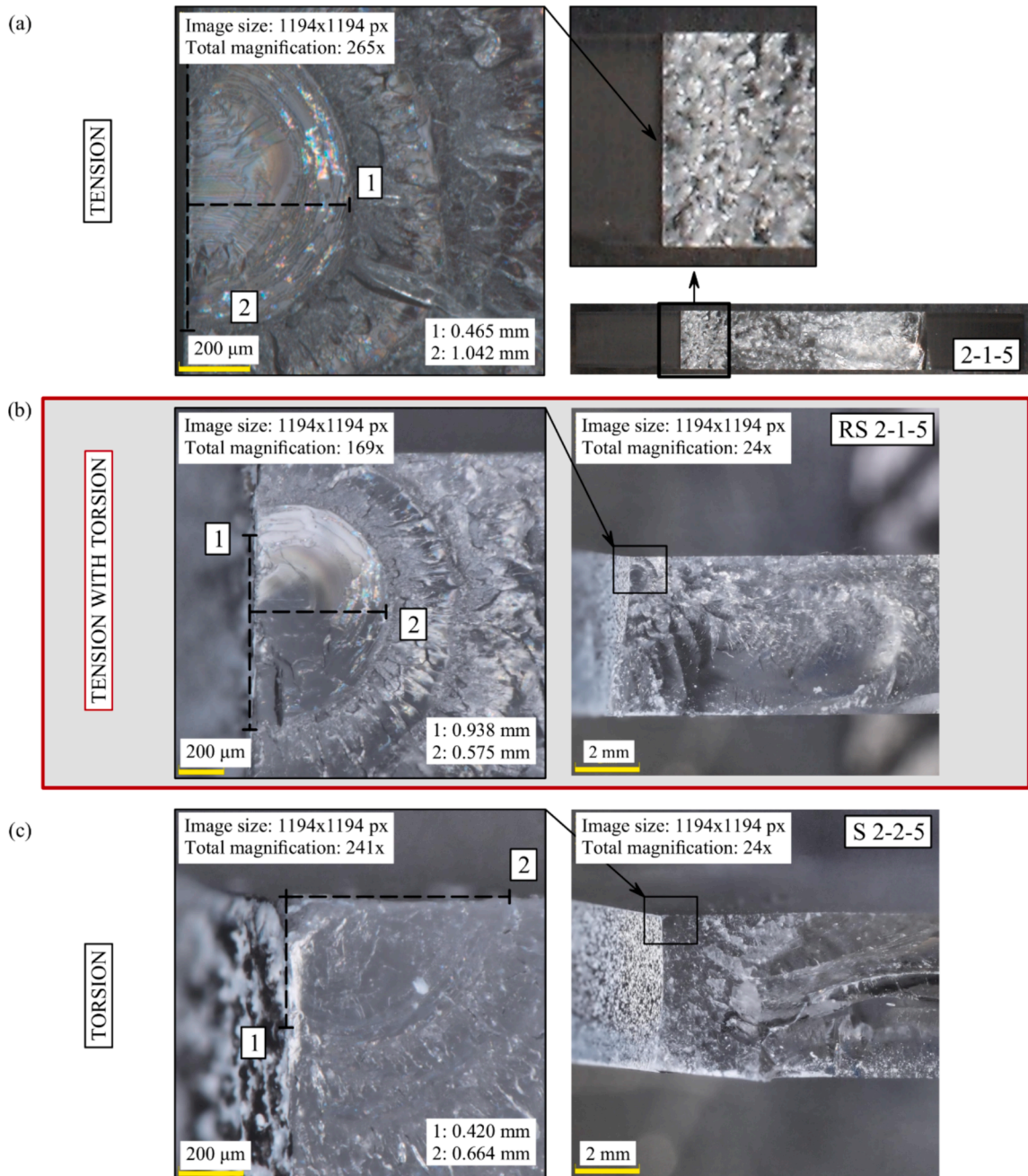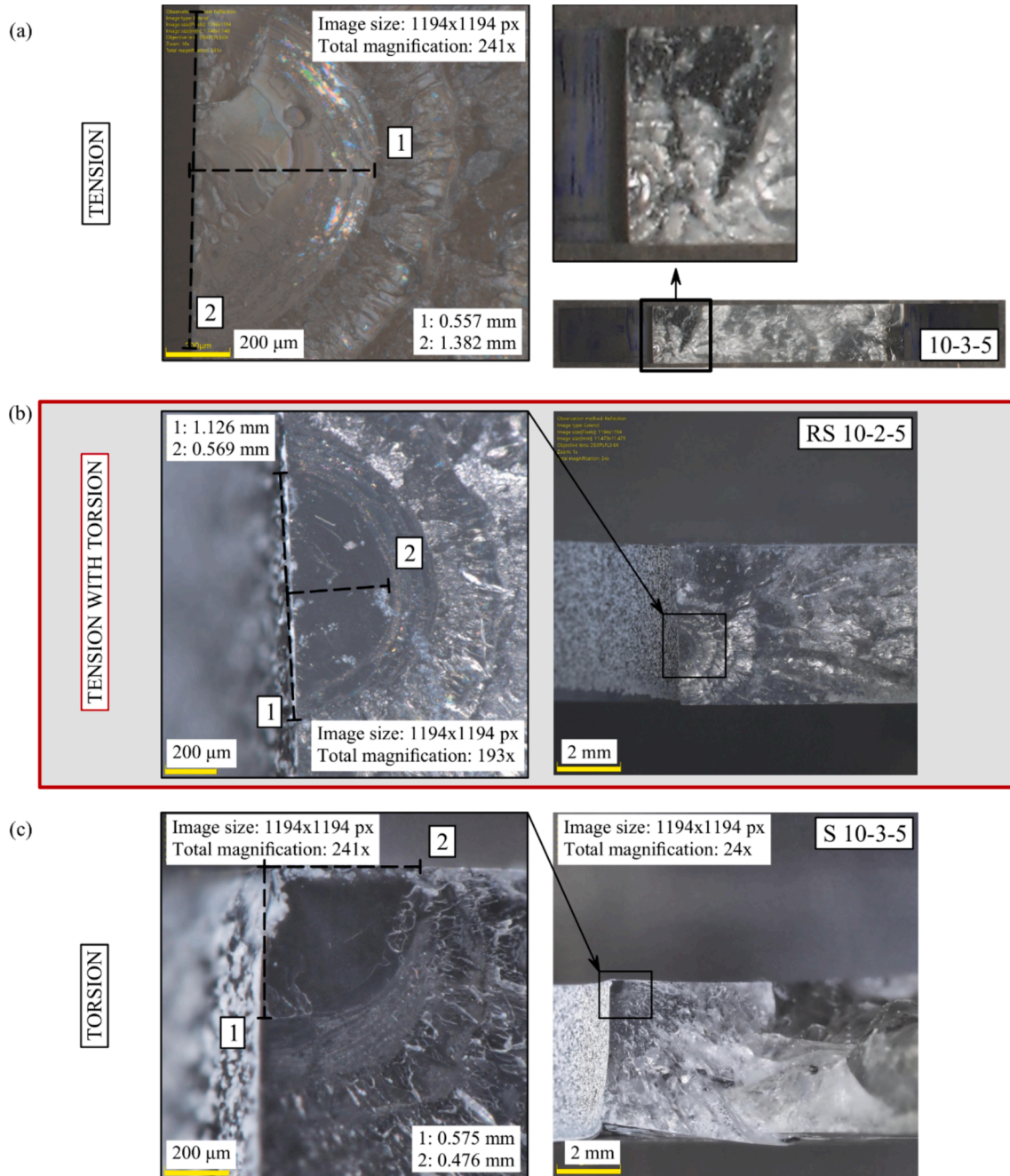
Fig. 12. Microscopic images of fracture surfaces of specimens subjected to: a) tension [16], b) tension with torsion and c) torsion [16], weakened by V-notches with rounding radius ρ = 10 mm: places of crack initiation and their characteristic dimensions.
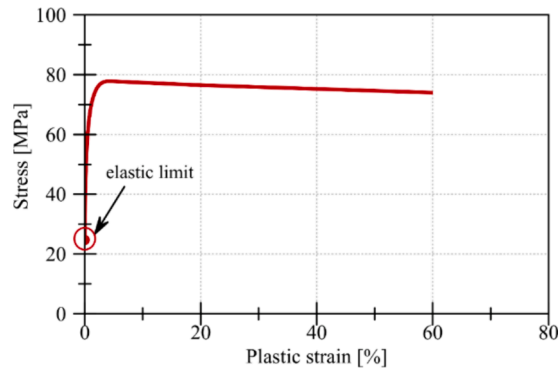
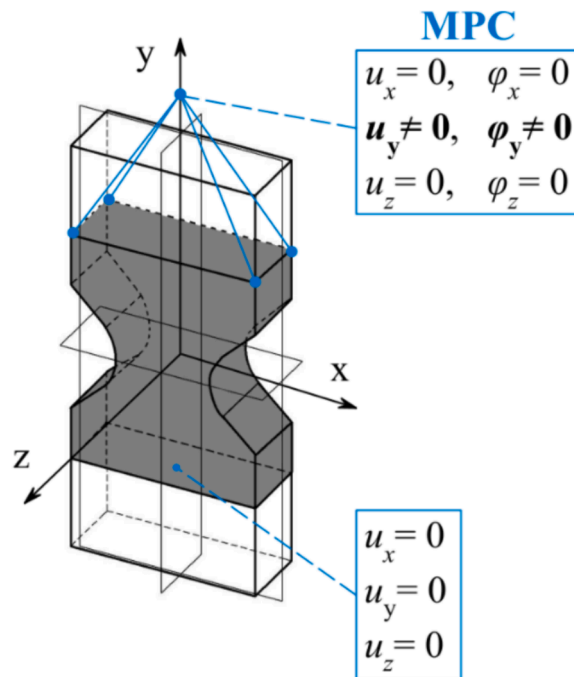**Fig. 13.** The hardening curve for Polymethyl methacrylate (PMMA).

Fig. 14. Boundary conditions used in the numerical calculation of a notched specimen subjected to tension with torsion.

PHANTOM cameras, each set to observe a different notch (Fig. 2c,d).

2.1. Material and specimens

The subjects of the study are flat specimens weakened with V-notches with different notch root radii $\rho = 0.5$, 2 and 10 mm. The shape of the specimens is shown in Fig. 3. The components were made from cast polymethylmethacrylate (PMMA) sheets in two thicknesses $g = 5$ and 15 mm. The basic properties of the PMMA tested were determined by the tests described in Bura and Seweryn [16]: Young's modulus $E = 3254$ MPa, tensile strength $R_{\mathrm{m}} = 72.10$ MPa, elastic limit $R_{0.05} = 24.51$ MPa and Poisson's ratio $\nu = 0.38$.

2.2. Experimental results of notched element fracture in uniaxial tensile test

As a tests result, the dependence of tensile force as a function of specimen base elongation (for $g = 5$ mm – Fig. 4a, and for $g = 15$ mm – Fig. 4b) and torsional moment as a function of specimen base twist angle (for $g = 5$ mm – Fig. 5a and for $g = 15$ mm – Fig. 5b). was obtained. The relevant numerical data are summarised in Table 2. In all cases, fracture occurred at lower critical load values than in the case of uniaxial conditions (Table 3), as described in the work of Bura and Seweryn [16]. Thus, the simultaneous action of two types of loading accelerated the crack initiation process. The nature of the torsion and tensile curves for all specimens, except those with a notch root radius of $\rho = 10$ mm, is close to linear. The smaller the notch root radius ρ, the fracture initiation occurred with a smaller
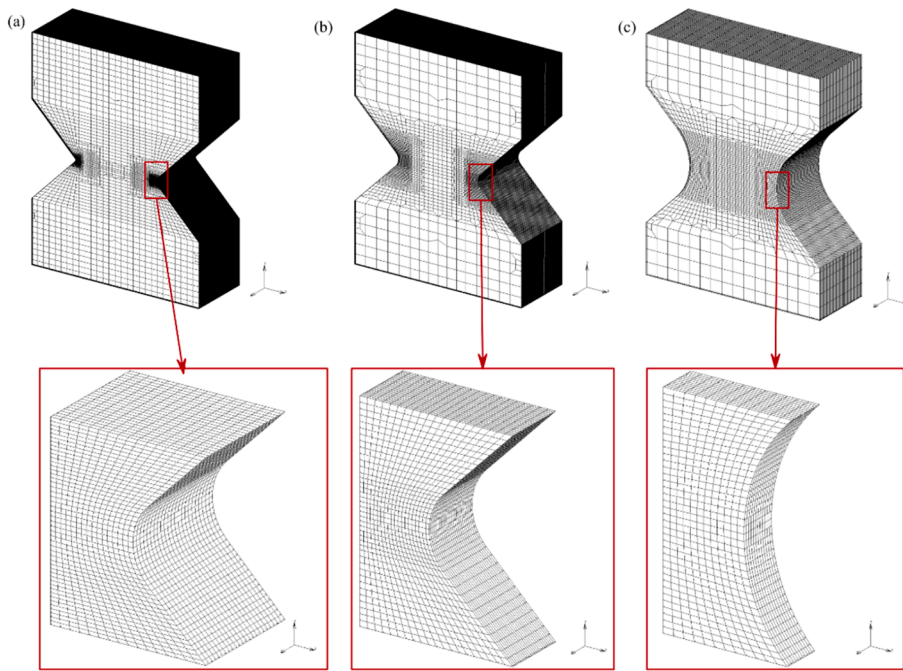
Fig. 15. Finite element meshes for notched specimens with root radius ρ equal to: (a) 0.5 mm, (b) 2 mm and (c) 10 mm.
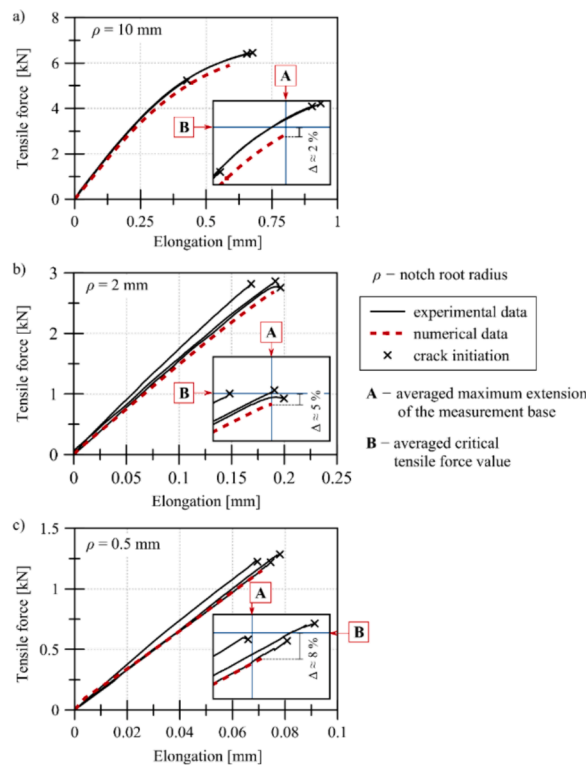

Fig. 16. Tensile curves of notched specimens with nominal thickness $g = 5$ mm and radius: (a) $\rho = 10$ mm, (b) $\rho = 2$ mm and (c) $\rho = 0.5$ mm. Black − experimental results, red − numerical results of biaxial tests.

Fig. 17. Torsional curves of notched specimens with nominal thickness $g = 5$ mm and radius: (a) $\rho = 10$ mm, (b) $\rho = 2$ mm and (c) $\rho = 0.5$ mm. Black – experimental results, red – numerical results of biaxial tests.
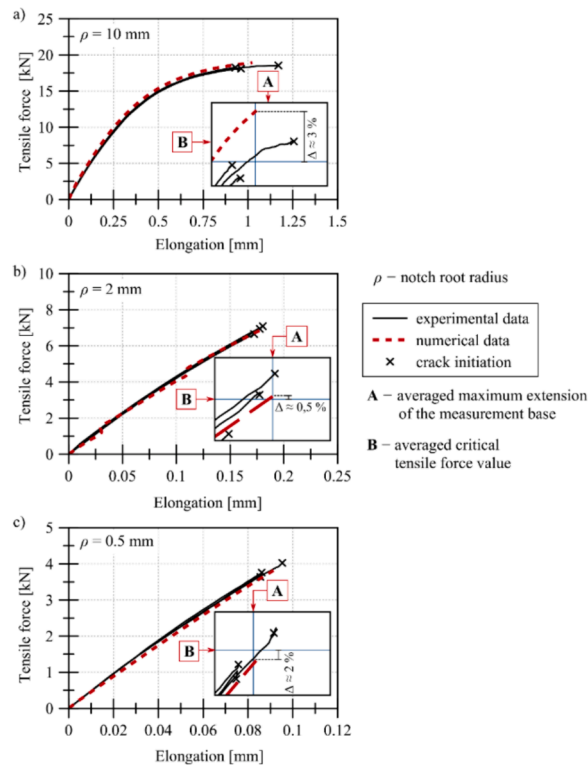
measurement base elongation and a smaller tensile force value. It should be noted that for the two smallest notch radii, fracture initiated at similar levels of gauge-base elongation regardless of specimen thickness g. As in the pure torsion test, for the biaxial loading condition, i.e. tensile with torsion, crack initiated at different levels of torsion angle of the gauge base.

The smaller the notch root radius ρ, the smaller the critical torsional angle value. In the case of a biaxial loading condition, the radius ρ also varied the critical torque value (as a reminder: in the case of pure torsion, very similar critical torsional torque values were obtained, irrespective of the notch root radius). The smaller the notch root radius, the smaller both the maximum torsional angle and the torsional torque value. Invariably, the smaller the cross-sectional dimensions of the specimen at the notch base, the more susceptible it is to torsion, even in tensile participation (thin specimens fractured at the larger notch base torsion angle). After the tests were carried out, the correctness of the selection of the speed of setting the angle of rotation of the measuring base was verified. For this purpose, critical load values from fracture tests in uniaxial (F^{I}, M_s^{III}) and biaxial ($F^{I/III}$, $M_s^{I/III}$) loading conditions were compared (Table 3).

As can be seen, the ratio of the m/f parameters determined from the experimental data is close to unity. Thus, it can be concluded that the adopted linear displacement velocity and rotation angle of the test base allowed the biaxial loading condition – torsion with tension – to be realised with similar proportions of both types of loading.

Using the data recorded by the ARAMIS 3D 4 M vision system, which was used for non-contact measurement of the elongation and torsion angle of the measurement base, Fig. 6 shows the equivalent strain fields distributions on the observed specimen wall. It can be seen that the largest deformations occur in the vicinity of the notch bottom, the larger the root radius and the thicker the specimen.

Figs. 7-9 show the specimens after the fracture tests carried out in the biaxial loading condition. In addition, these figures show example specimens of the same shape subjected to uniaxial tensile and also torsion tests, the results of which are described in the work of Bura and Seweryn [16]. The observed nature of the failure does not correspond to any of the previously studied uniaxial states [16]. The cracks form a more flattened area than in pure torsion (effect of tensile loading). The main branches arrange themselves in a near-triangular shape. The larger the notch root radius ρ, the later – with respect to the moment of crack initiation – the pronounced branching appears. The smaller the radius ρ, the arms of the main branches reach closer to the edge of the jaws of the testing machine. For specimens with notch root radius $\rho = 10$ mm, the image of the damaged specimen is similar to that obtained in the pure tensile test [16], but the angle of inclination of the crack initiation surface to the plane of notch symmetry is different.

The numerous cracks in the specimens definitely hampered the analysis of the fracture surfaces after the tensile-torsion tests. Figs. 10-12 show the nature of the fractures. The site of crack initiation assumes the shape of a semi-ellipse or its quadrant, which was respectively observed in the fractures of specimens subjected to pure tension and pure torsion [16]. The characteristic smooth surfaces occurring in the form of a quarter ellipse are cracks that initiated from the edge of the specimen or from very close to it. There is
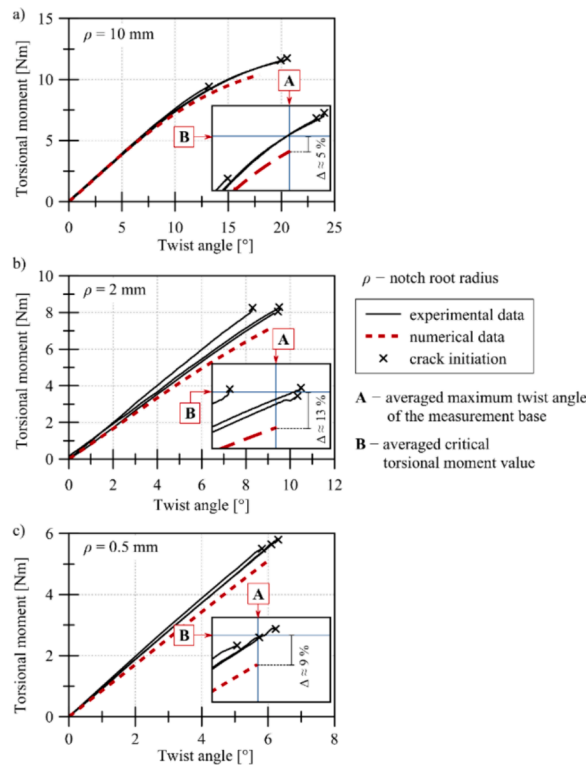
Fig. 18. Tensile curves of notched specimens with nominal thickness $g = 15$ mm and radius: (a) $\rho = 10$ mm, (b) $\rho = 2$ mm and (c) $\rho = 0.5$ mm. Black – experimental results, red – numerical results of biaxial tests.

therefore a relationship between the location of the crack initiation site and the loading conditions. The torsional moment leads to crack initiation from the edge of the specimen, the tensile force induces a crack from near the centre of the specimen thickness, and in the case of the complex condition we are dealing with an intermediate situation, i.e. the prediction of the crack initiation location should concern the area between the main symmetry plane of the specimen and its lateral surface.

3. FEM Modeling

Numerical calculations were carried out using the finite element method in the MSC Marc Mentat 2021.1 (build 800397, 2021/03/19). The environment of this program was used for all stages of FEM analysis, also for pre- and postprocessing. The general-purpose finite element method analysis code was used. PMMA was described by an elastic–plastic material model with isotropic hardening rule and von Mises plasticity condition. The linear elastic range is described by the generalised Hooke's law, which assumes values of Young's modulus $E = 3254$ MPa and Poisson's ratio $v = 0.38$. The above were determined in tensile tests on paddle specimens [16]. The stress–strain relationship in the plastic part was described by a hardening curve (Fig. 13) established by a hybrid method involving the identification of the actual material hardening curve from iterative FEM calculations. The process of establishing this relationship is discussed in more detail in the work of Bura and Seweryn [16]. Numerical models of the specimens were prepared using spatial HEX8 elements, the given boundary conditions are shown in Fig. 14. Fig. 15 shows the subdivision grids for the completed elements. The convergence of the numerical solution is described in [44].

3.1. FEM results

Numerical calculations for specimens subjected to tension with torsion were carried out by controlling the torsion angle and displacement of the specimen, until the maximum torsion angle of the gauge base determined in the experimental tests was reached (Table 2). As a result of the numerical calculations carried out, tensile curves, i.e. the dependence of the tensile force and the elongation of the gauge base, and torsional curves, i.e. the dependence of the torsional moment as a function of the gauge base twist angle, were obtained. The results of the numerical calculations were compared with the experimental data (Fig. 16- 19). The relative error between the critical tensile force value and the experimentally determined average tensile force value (value marked with "B") for specimens of nominal thickness $g = 5$ mm is 2–8 % (Fig. 16), and 0.5–3 % for specimens of nominal thickness $g = 15$ mm (Fig. 18). Relative error values were also determined for the critical torsional torque value in relation to the experimentally determined average torque value (value marked with the letter "B"). For specimens with a nominal thickness of $g = 5$ mm, the error in this case is 5–13 % (Fig. 17), while
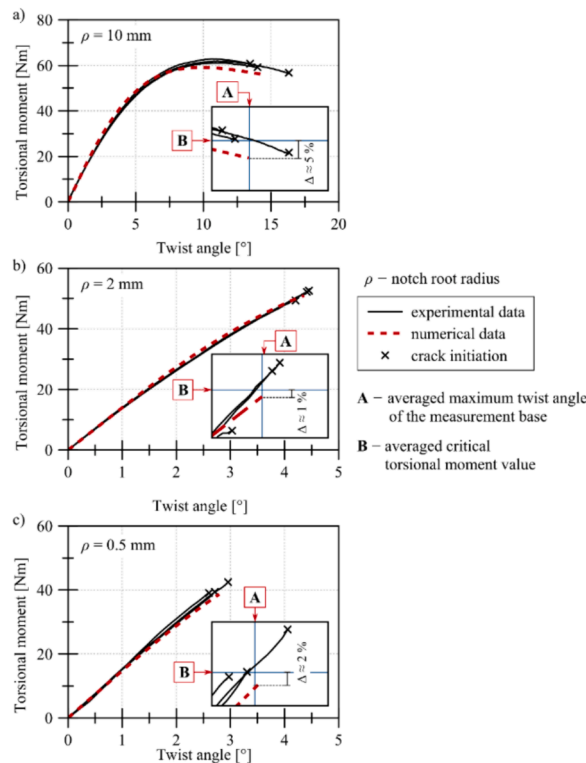
Fig. 19. Torsional curves of notched specimens with nominal thickness $g = 15$ mm and radius: (a) $\rho = 10$ mm, (b) $\rho = 2$ mm and (c) $\rho = 0.5$ mm. Black − experimental results, red − numerical results of biaxial tests.

for specimens with a nominal thickness of $g = 15$ mm, it is 1–5 % (Fig. 19). A high convergence between numerical results and experimental data was obtained. For thicker specimens, the value of the relative error is considerably lower.

As a result of the numerical calculations, the distributions of maximum principal stress and maximum principal plastic strain at the time of reaching the critical load value (experimentally averaged value for a given specimen type) were obtained. The stress and strain fields are shown on the undeformed specimens in Fig. 20 and Fig. 21. Fig. 20 shows the distributions of maximum principal stress σ_1 for all tested specimens.

The maximum normal stress values are similar for most specimen types and occur near the notch bottom near its edge. A gentle increase in the maximum value of σ_{max} in the specimen is observed as the notch root radius ρ decreases.

Fig. 21 shows the maximum plastic strain ε_1^p distribution. The highest strain values were located at the notch bottom. The larger the notch root ρ, the larger the maximum plastic strain value ε_{max}^p and, at the same time, the larger the yield zone. The highest maximum plastic strain values were observed in notched specimens with notch radius $\rho = 10$ mm. At the same time, the thicker the specimen, the higher the strain values. The locations of the points where the maximum stress and plastic strain values were indicated varied with the notch root radius and the specimen thickness. Experimental investigations proved that during tension with torsion, in most cases the crack initiated from the region of the notch bottom and the lateral surface of the specimen. For specimens with notches with a radius of $\rho = 10$ mm, the initiation points occurred closer to the centre of the specimen thickness and were significantly distant from the notch bottom. Table 4 describes the location of the points at which the maximum values of principal stress σ_1 and plastic strain ε_1^p occurred, where: x_m is the distance of the point from the notch surface and z_m is the distance of the point from the side surface of the specimen measured on a plane parallel to the notch symmetry plane and offset by y_m. For each specimen type, two points of σ_{max} and ε_{max}^p were indicated, one on each half of the specimen (Fig. 22).

The points of occurrence of the maximum values of stress and plastic strain were determined by cross-sections in which the variation of these values as a function of specimen thickness and as a function of the distance between notches was analysed. The maximum value of normal stress σmax (Fig. 23 for $g = 5$ mm and Fig. 24 for $g = 15$ mm) is not reached at the same point for each radius ρ.

In the case of thinner specimens (Fig. 23), the smaller the radius ρ, the higher the maximum stress value σ_{max} is and located closer to the specimen sidewall (Fig. 23a) and the notch surface (Fig. 23b). When $\rho = 10$ mm, the maximum stress value appears at the centre of the specimen thickness. Analysing the distribution of σ_1 as a function of the distance between notches, as many as two locations of the maximum σ_{max} value are noted. The locations of these points are similar to the locations of the experimental crack initiation points (Figs. 10–12). The stress distribution σ1 for the specimen with the largest notch root radius ρ is close to symmetrical with respect to the main symmetry planes of the specimen, while in the other cases a significant decrease in stress values is observed at the opposite side
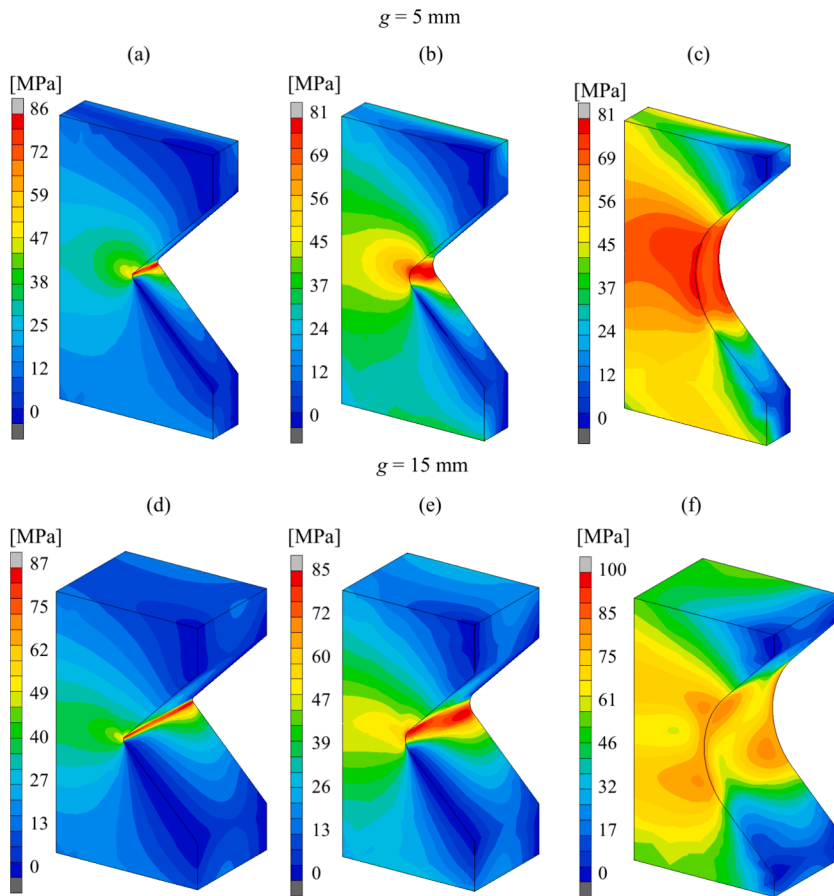
g = 5 mm

g = 15 mm

Fig. 20. Maximum principal stress σ_1 distribution in specimens with notch root radius ρ equal to: (a), (d) 0.5 mm, (b), (e) 2 mm and (c), (f) 10 mm (tensile with torsion).

wall of the specimen. Similar trends are observed for specimens with a nominal thickness of $g = 15$ mm (Fig. 24), except for the one with the largest notch radius.

The distributions of plastic strain ε_1^p by specimen thickness and by distance between notches are shown in Fig. 25 and Fig. 26 for the thinner and thicker specimens, respectively. For specimens with nominal thickness $g = 5$ mm, the distributions are close to symmetrical with respect to the main specimen symmetry planes. The maximum value of strain ε_{max}^p occurs in the vicinity of the specimen sidewall (Fig. 25a) and moves closer to the sidewall surface the smaller the notch root radius. The values of plastic strain ε_1^p decrease dramatically after reaching the maximum. The opposite is true for the distribution of this strain along the distance between notches (Fig. 25b) – large strain gradients are observed near the notch bottom. In this case, the values are again distributed almost symmetrically. The red markers in the figure indicate the maximum values, but the differences between the plastic strain values in the opposite notches are small enough that both locations can be considered as potential sites for crack initiation.

By analysing the plastic strain distributions for specimens with a nominal thickness of $g = 15$ mm (Fig. 26), similar conclusions can be drawn to those for thinner specimens. Again, the larger the notch root radius ρ, the further the point of occurrence of the ε_{max}^p maximum is from the lateral surface of the specimen (Fig. 26a). For notched specimens with a radius of $\rho = 10$ mm, the maximum of this strain occurs ideally in the centre of the specimen thickness. The obtained values of σ_{max} and ε_{max}^p in the following section were used to formulate a stress–strain fracture criterion.

4. Fracture predictions

As a result of the numerical calculations carried out, the stress and strain distributions under the critical loading conditions were obtained. The calculations made it possible to identify the locations of the maximum values of the highest principal stress and the highest principal plastic strain (σ_{max} and ε_{max}^p, respectively). These locations were considered as potential crack initiation sites and the data obtained were used to formulate a fracture criterion. Table 5 and Table 6 show the values of stress σ_1 and the corresponding values of plastic strain ε_1^p measured at the point of occurrence of maximum stress σ_{max} and maximum plastic strain ε_{max}^p at the time of fracture initiation during tensile-torsion (Table 5 and Table 6). The values of maximum principal stress and maximum principal plastic strain measured at the points of maximum normal stress and plastic strain obtained from the numerical calculations are shown in Fig. 27. It
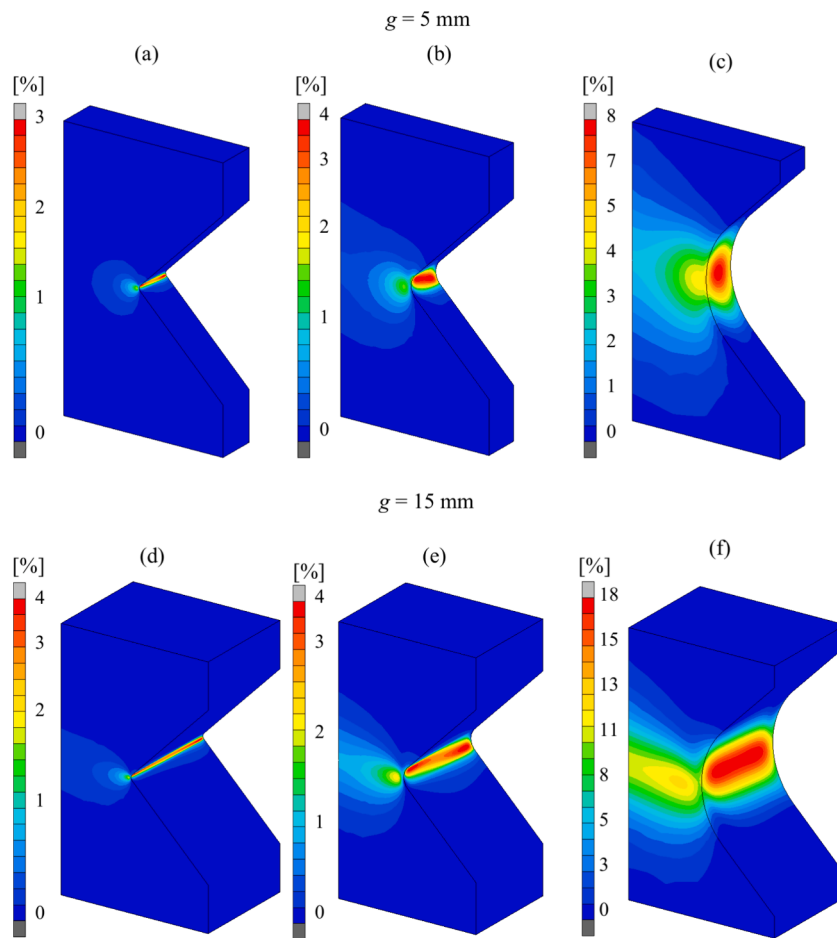
g = 5 mm

g = 15 mm

Fig. 21. Maximum principal plastic strain ε_1^p distribution in specimens with notch root radius ρ equal to: (a), (d) 0.5 mm, (b), (e) 2 mm and (c), (f) 10 mm (tensile with torsion).

Table 4
Location of occurrence of stress and plastic strain maxima − numerical calculations.

Notch root radius ρ [mm]	Averaged specimen thickness g [mm]	Maximum stress σ_{max} – location point [mm]			Maximum plastic strain ε_{max}^p – location point [mm]		
		x_m	y_m	z_m	x_m	y_m	z_m
0.5	4.92	0	0.19	0.41	0	0.26	0.51
	14.5	0.06	0.28	0.87	0	−0.24	0.71
2	4.92	0	−0.39	1.23	0.15	0.94	0.82
	14.5	0	−0.77	1.35	0.15	0.94	1.66
10	4.92	2.46	0	2.46	0	0	2.46
	14.5	10.00	0	7.25	0	−0.41	3.73

was determined in which cases the location of the maximum stress σ_{max} or plastic strain ε_{max}^p coincides (or is close) with the experimentally verified location of the crack initiation site (Figs. 10–12) – points marked in red. The data from these points were then adopted in establishing the form of the fracture criterion.

The resulting relationships of highest principal stress and highest principal plastic strain measured at the points of occurrence of the maximum of these values can be described by a linear function, and the fracture criterion can take the form proposed in the work of Bura and Seweryn [44] The quoted relationship assumes that normal stress and plastic strain (the largest principal) are responsible for crack initiation, and that these influence the material's resistance to fracture (measured by the critical value of normal stress). The higher the level of plastic strain, the lower the resistance. Thus, the stress–strain criterion for fracture can take the form in this case [44]:
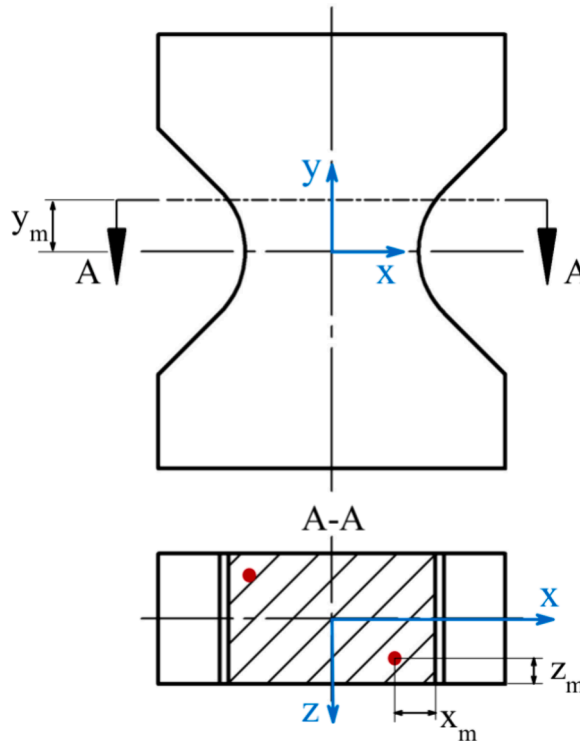
Fig. 22. Location of points (red dots) of occurrence of maximum values of monitored quantities (stress and plastic strain maxima) on the example of a notched sample.

$$\max_{(n,x_0)} \frac{\sigma_n}{\sigma_c} = \max_{(n,x_0)} \frac{\sigma_n}{\sigma_{c0}(1-\omega)} = 1 \tag{1}$$

where: σ_n – the normal stress on the physical plane, σ_c – the failure stress in the damaged material, σ_{c0} – the failure stress in the undamaged material, x_0 – the vector defining the location of crack initiation, n – the vector normal to the physical plane, ω - damage state variable. The damage variable ω can be described as the ratio of the value of the highest plastic strain ε_1^p and the critical value of plastic strain ε_c, namely:

$$\omega = \frac{\varepsilon_1^p}{\varepsilon_c} \tag{2}$$

In the work cited above, the stress–strain criterion was successfully used to predict the fracture of planar notched PMMA components subjected to simple loading states, i.e. uniaxial tension and torsion [16,44]. This paper shows that a similar form of the criterion can be used to predict fracture processes under biaxial loading condition i.e. tension with torsion. In order to obtain the full form of the criterion, the values of the critical parameters of stress σ_{c0} and plastic strain ε_c were determined, which were: $\sigma_{c0} = 97.99$ MPa, $\varepsilon_c = 0.2865$, respectively. The above criterion was verified and the verification results in the form of relative error between the stress value obtained from the σ_c criterion and the value obtained from the numerical calculations are summarised in Table 7. A similar form of the criterion was used by Derpeński and Seweryn [45,46] to predict fracture in axisymmetric tests made of aluminium alloy subjected to tensile torsion. The authors proposed to include in the criterion not only maximum normal stresses, but also tangential stresses depending on plastic deformation.

The data presented for tensile-torsion presented in this work and the data presented in the works [16,44] concern the same types of specimens and PMMA from the same batch, so it was decided to compare them. Analysing the individual linear functions used to describe the relationship between the highest principal stress and the highest principal plastic strain, it should be noted that for tensile and tensile-torsion these functions take on similar parameter values. Only the relationship of these quantities for torsion specimens apparently differs. Thus, Fig. 28 shows the relationship between the highest principal stress and the highest principal plastic strain for all the load states tested. It is noted that the data points obtained for the twisted elements, which exhibited significantly higher levels of plastic strain at the time of crack initiation, deviate from the linear relationship represented by the other points, so the points in question are described by two linear functions. One trend line refers to the data (values of the highest principal stress and the highest principal plastic strain) obtained for uniaxial tension and torsion with tension, while the other trend line describes the points collected from the torsional fracture analysis. The point of intersection of the lines was considered as the limit of applicability of one and the other relationship. The critical values of the parameters σ_{c0} and ε_c were for strains equal to or no greater than $\varepsilon_{gr} = 0.0491$:
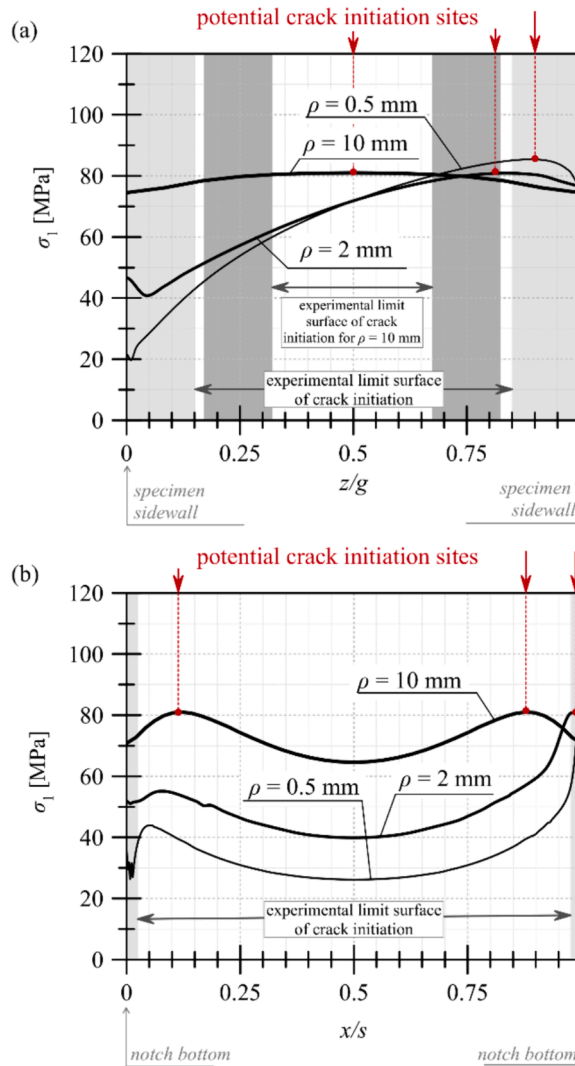
Fig. 23. Maximum principal stress σ_1 distribution for specimens with nominal thickness $g = 5$ mm: (a) along the specimen thickness − for x_m, y_m (z − distance from the specimen side surface, g − nominal specimen thickness), (b) along the specimen width − for z_m, y_m (r − distance from the bottom of the notch, s − distance between notches).

- $\sigma_{c0} = 102.26$ MPa, $\varepsilon_c = 0.2820$

and for strains greater than $\varepsilon_{gr} = 0.0491$:

- $\sigma_{c0} = 85.98$ MPa, $\varepsilon_c = 2.7420$.

The above form of the criterion was verified by calculating the relative error between the stress value determined on the basis of the σ_c relation discussed above and the value obtained from the numerical-experimental analysis. The values obtained are summarised in Table 8. An average relative error of 8 % was obtained. The error values are larger than for the criteria relating to each state separately, but are still at a satisfactory level. This approach will make it possible to effectively predict fracture in flat notched specimens made of PMMA regardless of the specimen thickness, the notch root radius and the loading condition (tension, torsion, tension with torsion). Improvements in the results obtained may be possible following refinement of the numerical model (selection of a different material model), i.e. improving the convergence of experimental results and numerical calculations. Bura et al. [47] used classical brittle fracture criteria in combination with the equivalent material concept (EMC) [48] and the fictitious material concept (FMC) [49] to predict fracture in notched specimens, also described in this paper, subjected to uniaxial tension. The paper shows that both concepts yield significantly better results than using the basic forms of the MTS criterion [50] or the MS criterion [51]. However, it was pointed out that, depending on the size of the notch root radius and thus the size of the plastic zone, the effectiveness of EMC and FMC varies. The form of the criterion presented in this paper can be effectively used to predict fracture irrespective of the notch root radius, the

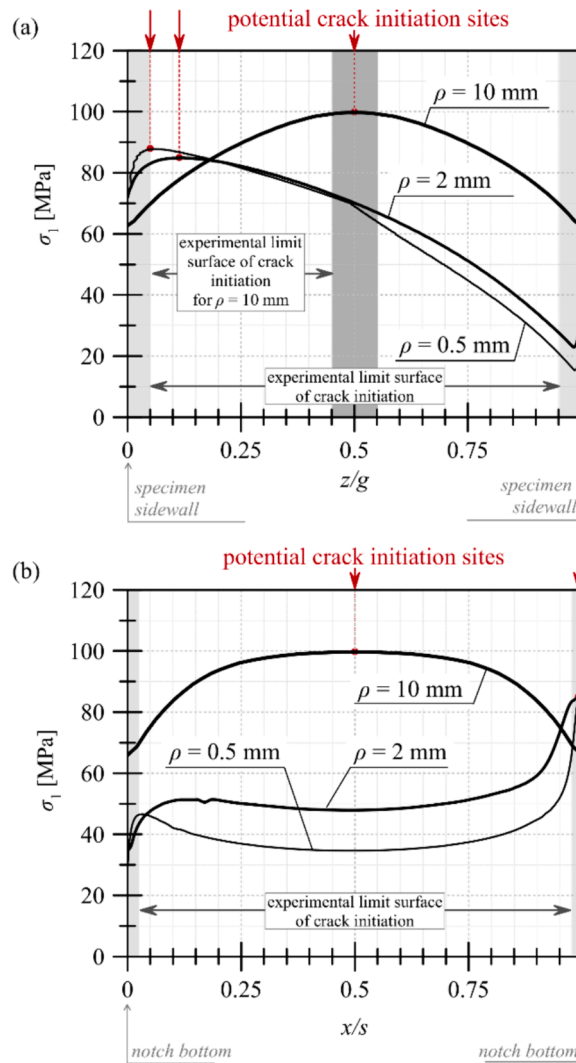**Fig. 24.** Maximum principal stress σ_1 distribution for specimens with nominal thickness $g = 15$ mm: (a) along the specimen thickness − for x_m, y_m (z − distance from the specimen side surface, g − nominal specimen thickness), (b) along the specimen width − for z_m, y_m (r − distance from the bottom of the notch, s − distance between notches).
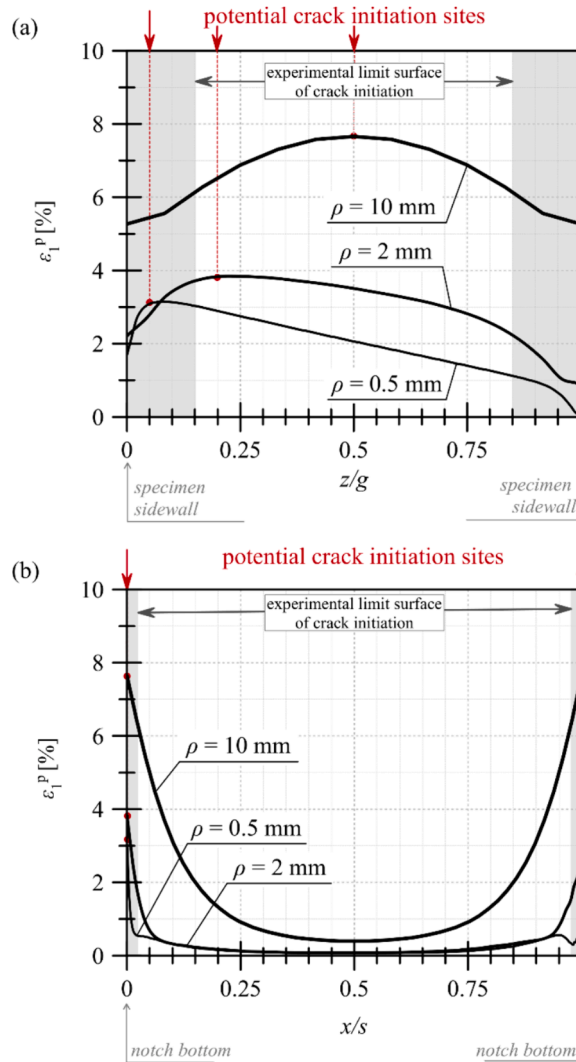
Fig. 25. Maximum principal plastic strain ε_1^p distribution for specimens with nominal thickness $g = 5$ mm: (a) along the specimen thickness − for x_m, y_m (z − distance from the specimen side surface, g − nominal specimen thickness), (b) along the specimen width − for z_m, y_m (r − distance from the bottom of the notch, s − distance between notches).

Fig. 26. Maximum principal plastic strain ε_1^p distribution for specimens with nominal thickness $g = 15$ mm: (a) along the specimen thickness − for x_m, y_m (z − distance from the specimen side surface, g - nominal specimen thickness), (b) along the specimen width − for z_m, y_m (r − distance from the bottom of the notch, s − distance between notches).
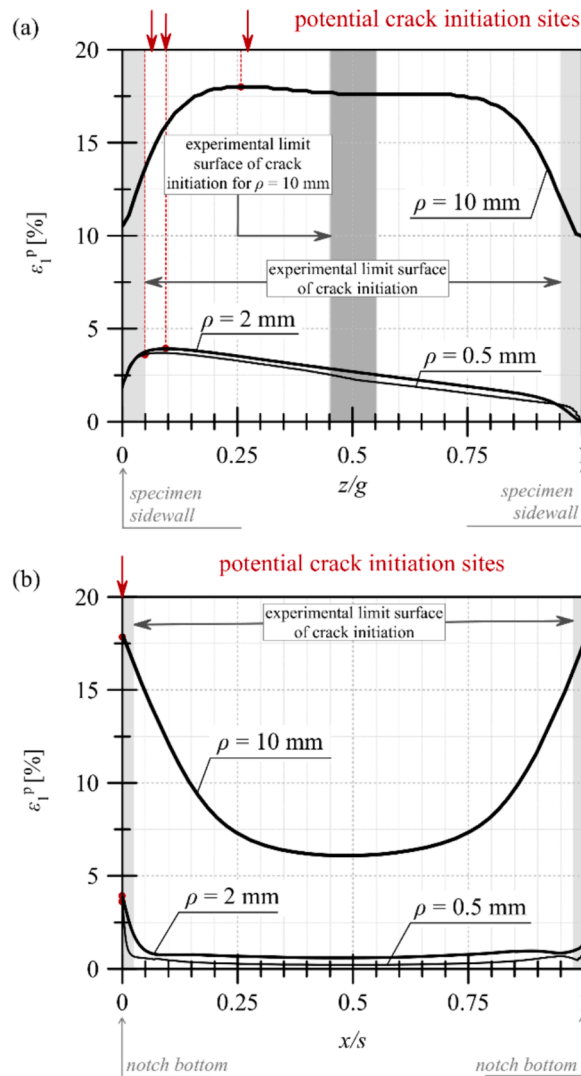
Table 5

Values of stress σ_1 and corresponding plastic strain ε_1^p measured at the point of occurrence of maximum stress σ_{max} at the time of crack initiation.

Notch root radius ρ [mm]	Averaged specimen thickness g [mm]	Stress [MPa]	Strain [%]
		σ_{max}	ε_1^p
0.5	4.92	85.40	3.08
	14.5	87.77	2.68
2	4.92	80.89	2.71
	14.5	84.87	3.05
10	4.92	80.98	2.54
	14.5	99.71	3.23

thickness of the specimen or the loading condition (tension, torsion and also proportional tension with torsion).

This stress–strain fracture criterion was used to determine the critical load values. For this purpose numerical calculations in tension, torsion and tension–torsion of the test specimens were carried out until its conditions were met at any node of the specimen model. For a given load, the values of maximum principal stress σ_1 and maximum principal plastic strain ε_1^p were read at each node. The value of the critical stress σ_c was then determined. If the stress σ_1 at a given node was greater than or equal to:

Table 6
Values of stress σ_1 and corresponding plastic strain ε_1^p measured at the point of occurrence of maximum plastic strain ε_{max}^p at the time of crack initiation.

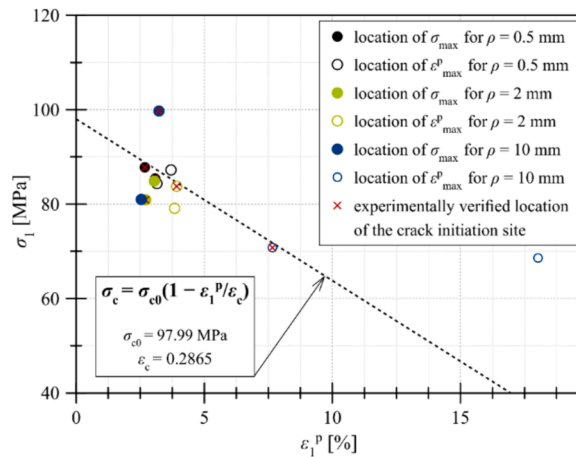| Notch root radius ρ [mm]	Averaged specimen thickness g [mm]	Stress [MPa] σ_1	Strain [%] ε_{max}^p
0.5	4.92	84.35	3.15
	14.5	87.23	3.70
2	4.92	79.10	3.84
	14.5	83.76	3.92
10	4.92	70.78	7.66
	14.5	68.59	18.03

Fig. 27. The maximum principal stress σ_1 as a function of: (a) the maximum principal plastic strain ε_1^p. Numerical results for tensile torsion read from the points of occurrence of σ_{max} and ε_{max}^p.

Table 7
Values of stress σ_1 and corresponding plastic strain ε_1^p measured at the point of occurrence of maximum stress σ_{max} and plastic strain ε_{max}^p and relative error.

ρ [mm]	g [mm]	The point of maximum stress σ_{max} value* σ_{max} [MPa]	ε_1^p [%]	The point of maximum plastic strain ε_{max}^p value** σ_1 [MPa]	ε_{max}^p [%]	The failure stress [MPa] $\sigma_c = \sigma_{c0}(1 - \frac{\varepsilon_1^p}{\varepsilon_c})$	The relative error [%] * $|\sigma_{max} - \sigma_c| / \sigma_c$ ** $|\sigma_1 - \sigma_c| / \sigma_c$
0.5	4.92	**85.40**[1]	**3.08**[1]	84.35	3.15	87.46	2*
	14.5	**87.77**[1]	**2.68**[1]	87.23	3.70	88.84	1*
2	4.92	**80.89**[1]	**2.71**[1]	79.10	3.84	88.73	9*
	14.5	84.87	3.05	**83.76**[1]	**3.92**[1]	84.58	1**
10	4.92	80.98	2.54	**70.78**[1]	**7.66**[1]	71.78	1**
	14.5	**99.71**[1]	**3.23**[1]	68.59	18.03	86.93	15*

[1]Data from the experimentally verified location of the crack initiation site.

$$\sigma_c = 102.26 \cdot (1 - \frac{\varepsilon_1^p}{0.2820}), \text{ for } \varepsilon_1^p \leqslant 0.0491,$$

$$\sigma_c = 85.98 \cdot (1 - \frac{\varepsilon_1^p}{2.7420}), \text{ for } \varepsilon_1^p > 0.0491,$$

(3)

the load was considered to be the critical load and the calculation was terminated. The obtained critical tensile force (Fig. 29) and torsional moment (Fig. 30) values for all tested specimens and the loading type were compared with the experimentally obtained values. An average relative error of 17 % was obtained, which, according to the authors, is still a satisfactory result, as the predictions for most of the specimens are well below this error. The authors will certainly continue to work on the criterion form in order to obtain even better results.
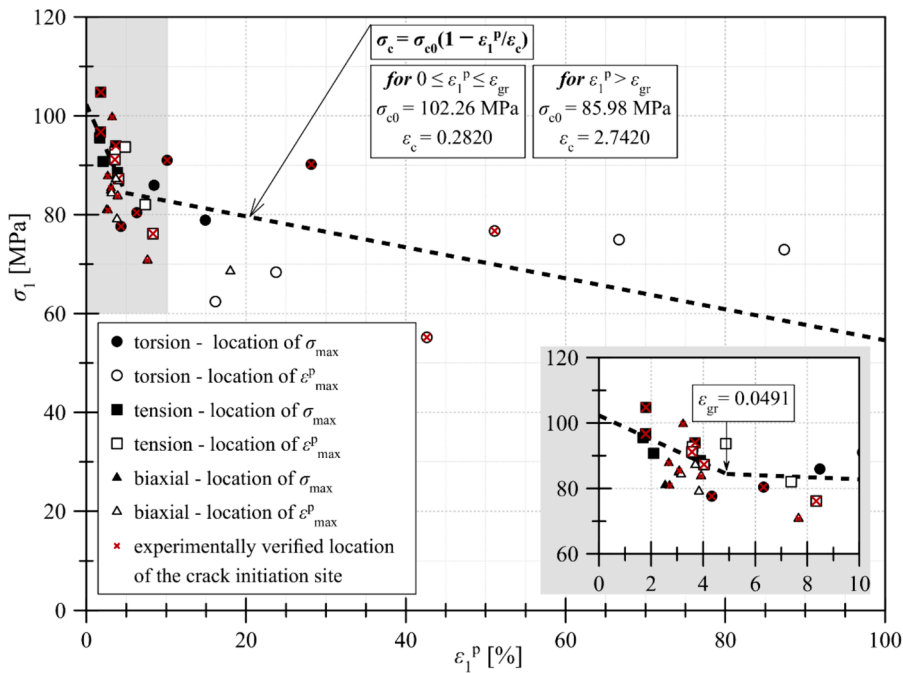
Fig. 28. Critical values of the maximum principal stress σ_1 as a function of the maximum principal plastic strain ε_1^p. Numerical results for all load cases read from the points of occurrence of σ_{max} and ε_{max}^p. Data for uniaxial tension and torsion obtained from the work of Bura and Seweryn [44].

Table 8
Values of stress σ_1 and corresponding plastic strain ε_1^p measured at the point of occurrence of maximum stress σmax and plastic strain $\varepsilon pmax$ and relative error for all loading conditions (Fig. 27).

ρ [mm]	g [mm]	The point of maximum stress σ_{max} value*		The point of maximum plastic strain ε_{max}^p value**		The failure stress [MPa]	The relative error [%]
		σ_{max} [MPa]	ε_1^p [%]	σ_1 [MPa]	ε_{max}^p [%]	$\sigma_c = \sigma_{c0}(1 - \frac{\varepsilon_1^p}{\varepsilon_c})$	*| $\sigma_{max} - \sigma_c$ | / σ_c **| $\sigma_1 - \sigma_c$ | / σ_c
Tension [44]							
0.5	4.92	**96.71**[1]	**1.79**[1]	92.70	3.59	95.79	1*
	14.5	**104.78**[1]	**1.80**[1]	93.69	4.87	95.73	9*
2	4.92	90.74	2.10	**87.30**[1]	**4.03**[1]	87.63	0**
	14.5	95.54	1.69	**91.15**[1]	**3.71**[1]	89.30	2**
10	4.92	88.52	3.89	**78.16**[1]	**8.35**[1]	83.36	9**
	14.5	**93.95**[1]	**3.69**[1]	82.05	7.41	88.88	6*
Torsion [44]							
0.5	4.92	**90.18**[1]	**28.15**[1]	72.93	87.37	77.15	17*
	14.5	**91.01**[1]	**10.12**[1]	74.95	66.69	82.80	10*
2	4.92	**80.41**[1]	**6.32**[1]	68.37	23.75	84.00	4*
	14.5	85.95	8.48	**76.71**[1]	**51.11**[1]	69.95	10**
10	4.92	**77.63**[1]	**4.33**[1]	62.43	16.16	86.54	10*
	14.5	78.90	14.90	**55.20**[1]	**42.63**[1]	72.61	24**
Tension with torsion							
0.5	4.92	**85.40**[1]	**3.08**[1]	84.35	3.15	91.09	6*
	14.5	**87.77**[1]	**2.68**[1]	87.23	3.70	92.55	5*
2	4.92	**80.89**[1]	**2.71**[1]	79.10	3.84	92.43	12*
	14.5	84.87	3.05	**83.76**[1]	**3.92**[1]	88.04	5**
10	4.92	80.98	2.54	**70.78**[1]	**7.66**[1]	83.57	15**
	14.5	**99.71**[1]	**3.23**[1]	68.59	18.03	90.53	10*

[1]Data from the experimentally verified location of the crack initiation site.

5. Conclusions

This paper presents the results of fracture experimental testing and numerical calculations flat PMMA notched specimens of different shape and thickness subjected to biaxial loading condition (tension + torsion), i.e. mixed-mode I + III. Digital image correlation (DIC) was used to measure the displacements on the surface of the specimens and, in particular, the twist angle of the
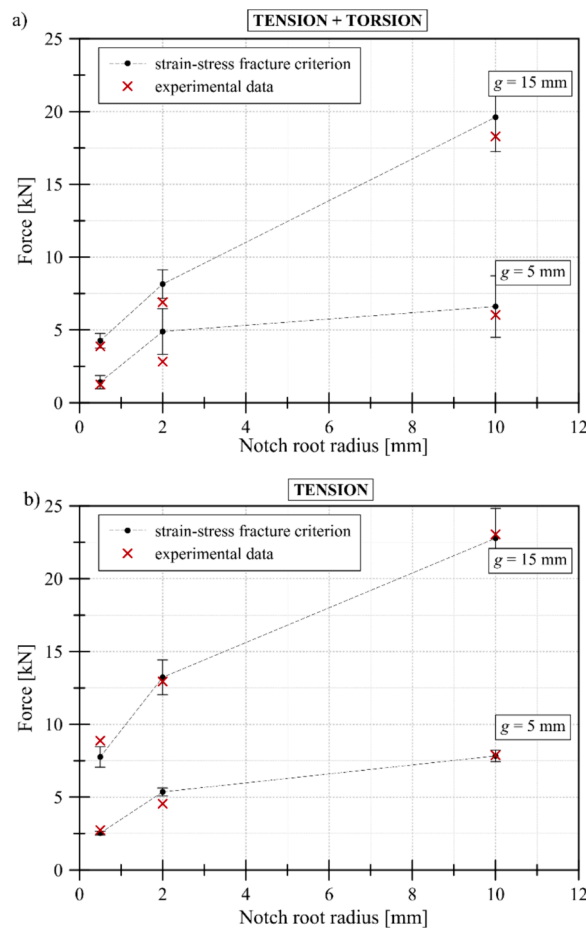
Fig. 29. Experimental and numerical critical tensile force values for: a) biaxial loading – tension with torsion and b) for uniaxial loading – tension.

measurement base. An important part of the study was not only the determination of critical load values, but also the location of the crack initiation site. Since the sites were located both in the notch bottom and at some distance from it, linear elastic models should not be used to predict fracture. This is especially true for specimens with larger notch root radii. Hence, numerical calculations with the finite element method uses an elastic–plastic model of the material and characterizes the hardening of the material already from the elastic limit (rather than the yield limit). This is important for small notch root radii, when the dominant load is tensile and there are small yield zones.

The stress–strain criterion of fracture was used to predict the fracture. This is because it was noted that normal stresses are responsible for crack initiation, the critical value of which depends on the value of plastic strain. This relationship is described by 2 straight lines, depending on the value of the largest principal plastic strain. Particularly satisfactory agreement of the prediction with the results of experimental tests carried out for tensile and tensile-torsion, where there are no large plastic deformations. Less accuracy applies to torsion specimens (larger plastic deformations), but then also the repeatability of experimental results is lower and there are difficulties in locating the place of crack initiation.

CRediT authorship contribution statement

Elżbieta Bura: Writing – original draft, Visualization, Methodology, Investigation, Funding acquisition, Data curation, Conceptualization. **Wojciech Grodzki:** Methodology, Investigation, Data curation. **Andrzej Seweryn:** Writing – review & editing, Supervision, Methodology, Conceptualization.

Declaration of competing interest

The authors declare that they have no known competing financial interests or personal relationships that could have appeared to influence the work reported in this paper.
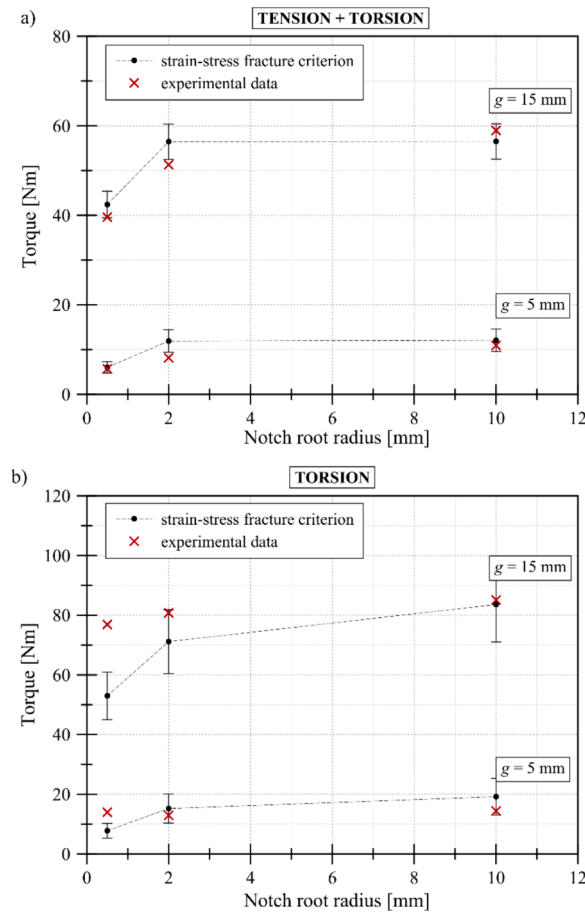
Fig. 30. Experimental and numerical critical torsional moment values for: a) biaxial loading – tension with torsion and b) for uniaxial loading – torsion.

Data availability

Data will be made available on request.

Acknowledgements

References

[1] Torabi AR, Abedinasab SM. Brittle fracture in key-hole notches under mixed mode loading: Experimental study and theoretical predictions. Eng Fract Mech 2015;134:35–53. https://doi.org/10.1016/j.engfracmech.2014.12.006.

[2] Seweryn A. Brittle fracture criterion for structures with sharp notches. Eng Fract Mech 1994;47(5):673–81. https://doi.org/10.1016/0013-7944(94)90158-9.

[3] Bura E, Seweryn A. Mode I fracture in PMMA specimens with notches – Experimental and numerical studies. Theor Appl Fract Mech 2018;97:140–55. https://doi.org/10.1016/j.tafmec.2018.08.002.

[4] Torabi AR, Shahbaz S, Cicero S, Ayatollahi MR. Fracture testing and estimation of critical loads in a PMMA-based dental material with nonlinear behavior in the presence of notches. Theor Appl Fract Mech 2022;118:103282. https://doi.org/10.1016/j.tafmec.2022.103282.

[5] Shahbaz S, Ayatollahi MR, Torabi AR, Cicero S. Fracture Behavior of Two Biopolymers Containing Notches: Effects of Notch Tip Plasticity. Appl Sci 2020;10(23): 8445. https://doi.org/10.3390/app10238445.

[6] M. R. Ayatollahi, M. Rashidi Moghaddam, S. M. J. Razavi, and F. Berto, "Geometry effects on fracture trajectory of PMMA samples under pure mode-I loading," *Eng Fract Mech*, vol. 163, pp. 449–461, Sep. 2016, doi: 10.1016/j.engfracmech.2016.05.014.

[7] Seweryn A, Łukaszewicz A. Verification of brittle fracture criteria for elements with V-shaped notches. Eng Fract Mech 2002;69(13):1487–510. https://doi.org/10.1016/S0013-7944(01)00138-2.

[8] Seweryn A, Poskrobko S, Mróz Z. Brittle fracture in plane elements with sharp notches under mixed-mode loading. J Eng Mech 1997;123(6):535–43. https://doi.org/10.1061/(ASCE)0733-9399(1997)123:6(535).

[9] Bura E, Derpeński Ł, Seweryn A. Fracture in PMMA notched specimens under compression – Experimental study. Polym Test 2019;77. https://doi.org/10.1016/j.polymertesting.2019.105923.

[10] E. Bura and A. Seweryn, "Fracture initiation in notched specimens subjected to compression: Strain rate effect," *Materials*, vol. 13, no. 11, 2020, doi: 10.3390/ma13112613.

[11] Ayatollahi MR, Torabi AR, Bahrami B. On the necessity of using critical distance model in mixed mode brittle fracture prediction of V-notched Brazilian disk specimens under negative mode I conditions. Theor Appl Fract Mech 2016;84:38–48. https://doi.org/10.1016/j.tafmec.2016.01.001.

[12] Torabi AR, Etesam S, Sapora A, Cornetti P. Size effects on brittle fracture of Brazilian disk samples containing a circular hole. Eng Fract Mech 2017;186: 496–503. https://doi.org/10.1016/j.engfracmech.2017.11.008.

[13] Li L, Zhang Y, Sun L, Hu H. Effects of strain rate and temperature on the mechanical behavior of polymethyl methacrylate (PMMA). Polym Bull 2023;80(8): 8685–702. https://doi.org/10.1007/s00289-022-04472-z.

[14] Torabi AR, Hamidi K, Rahimi AS, Cicero S. Notch fracture in polymeric specimens under compressive stresses: the role of the equivalent material concept in estimating the critical stress of polymers. Appl Sci 2021;11(5):2104. https://doi.org/10.3390/app11052104.

[15] Berto F, Elices M, Lazzarin P, Zappalorto M. Fracture behaviour of notched round bars made of PMMA subjected to torsion at room temperature. Eng Fract Mech 2012;90:143–60. https://doi.org/10.1016/j.engfracmech.2012.05.001.

[16] Bura E, Seweryn A. The fracture behaviour of notched PMMA specimens under simple loading conditions – Tension and torsion experimental tests. Eng Fail Anal 2023;148:107199. https://doi.org/10.1016/j.engfailanal.2023.107199.

[17] Berto F, Cendon DA, Lazzarin P, Elices M. Fracture behaviour of notched round bars made of PMMA subjected to torsion at −60°C. Eng Fract Mech 2013;102: 271–87. https://doi.org/10.1016/j.engfracmech.2013.02.011.

[18] Bahrami B, Ayatollahi MR, Ghouli S. Theory of critical distance combined with the generalized strain energy density criterion for mixed mode fracture assessment of PMMA dental materials. Procedia Struct Integrity 2020;28:829–35. https://doi.org/10.1016/j.prostr.2020.10.097.

[19] Ayatollahi MR, Aliha MRM, Hassani MM. Mixed mode brittle fracture in PMMA—An experimental study using SCB specimens. Mater Sci Engng A 2006;417 (1–2):348–56. https://doi.org/10.1016/j.msea.2005.11.002.

[20] Bahrami B, Ayatollahi MR, Gholizadeh AH, Mirzaei AM, Mehraban MR. Mixed mode brittle fracture prediction in cracks under frictional condition. Theor Appl Fract Mech 2024;129:104211. https://doi.org/10.1016/j.tafmec.2023.104211.

[21] Ayatollahi MR, Torabi AR. Investigation of mixed mode brittle fracture in rounded-tip V-notched components. Eng Fract Mech 2010;77(16):3087–104. https://doi.org/10.1016/j.engfracmech.2010.07.019.

[22] Ayatollahi MR, Torabi AR. Determination of mode II fracture toughness for U-shaped notches using Brazilian disc specimen. Int J Solids Struct 2010;47(3–4): 454–65. https://doi.org/10.1016/j.ijsolstr.2009.10.012.

[23] Aliha MRM, Samareh-Mousavi SS, Mirsayar MM. Loading rate effect on mixed mode I/II brittle fracture behavior of PMMA using inclined cracked SBB specimen. Int J Solids Struct 2021;232:111177. https://doi.org/10.1016/j.ijsolstr.2021.111177.

[24] Mousavi A, Aliha MRM, Imani DM. Effects of biocompatible Nanofillers on mixed-mode I and II fracture toughness of PMMA base dentures. J Mech Behav Biomed Mater 2020;103:103566. https://doi.org/10.1016/j.jmbbm.2019.103566.

[25] Mousavi SS, Aliha MRM, Imani DM. On the use of edge cracked short bend beam specimen for PMMA fracture toughness testing under mixed-mode I/II. Polym Test 2020;81:106199. https://doi.org/10.1016/j.polymertesting.2019.106199.

[26] Foti P, Razavi N, Berto F. Fracture assessment of U-notched PMMA under mixed mode I/II loading conditions by means of local approaches. Procedia Struct Integrity 2021;33:482–90. https://doi.org/10.1016/j.prostr.2021.10.055.

[27] Zhang R, Guo R, Wang S. Mixed mode fracture study of PMMA using digital gradient sensing method. Eng Fract Mech 2014;119:164–72. https://doi.org/10.1016/j.engfracmech.2014.02.020.

[28] Torabi AR, Shahbaz S, Ayatollahi MR. Fracture assessment of U-notched diagonally loaded square plates additively manufactured from ABS with different raster orientations. Eng Struct 2023;292:116537. https://doi.org/10.1016/j.engstruct.2023.116537.

[29] Ayatollahi MR, Aliha MRM. Analysis of a new specimen for mixed mode fracture tests on brittle materials. Eng Fract Mech 2009;76(11):1563–73. https://doi.org/10.1016/j.engfracmech.2009.02.016.

[30] Ayatollahi MR, Torabi AR. A criterion for brittle fracture in U-notched components under mixed mode loading. Eng Fract Mech 2009;76(12):1883–96. https://doi.org/10.1016/j.engfracmech.2009.04.008.

[31] Bidadi J, Aliha MRM, Akbardoost J. Development of maximum tangential strain (MTSN) criterion for prediction of mixed-mode I/III brittle fracture. Int J Solids Struct 2022;256:111979. https://doi.org/10.1016/j.ijsolstr.2022.111979.

[32] Aliha MRM, Bahmani A, Akhondi Sh. Numerical analysis of a new mixed mode I/III fracture test specimen. Eng Fract Mech 2015;134:95–110. https://doi.org/10.1016/j.engfracmech.2014.12.010.

[33] Ahmadi-Moghadam B, Taheri F. An effective means for evaluating mixed-mode I/III stress intensity factors using single-edge notch beam specimen. J Strain Anal Eng Des 2013;48(4):245–57. https://doi.org/10.1177/0309324713480767.

[34] Pirmohammad S, Kiani A. Study on fracture behavior of HMA mixtures under mixed mode I/III loading. Eng Fract Mech 2016;153:80–90. https://doi.org/10.1016/j.engfracmech.2015.12.027.

[35] Shen Z, Yu H, Guo L, Hao L, Zhu S, Huang K. A modified 3D G-criterion for the prediction of crack propagation under mixed mode I-III loadings. Eng Fract Mech 2023;281:109082. https://doi.org/10.1016/j.engfracmech.2023.109082.

[36] Liu S, Chao YJ, Zhu X. Tensile-shear transition in mixed mode I/III fracture. Int J Solids Struct 2004;41(22–23):6147–72. https://doi.org/10.1016/j.ijsolstr.2004.04.044.

[37] Chang J, Xu J, Mutoh Y. A general mixed-mode brittle fracture criterion for cracked materials. Eng Fract Mech 2006;73(9):1249–63. https://doi.org/10.1016/j.engfracmech.2005.12.011.

[38] Susmel L, Taylor D. The theory of critical distances to predict static strength of notched brittle components subjected to mixed-mode loading. Eng Fract Mech 2008;75(3–4):534–50. https://doi.org/10.1016/j.engfracmech.2007.03.035.

[39] Ayatollahi MR, Saboori B. A new fixture for fracture tests under mixed mode I/III loading. Eur J Mech A Solids 2015;51:67–76. https://doi.org/10.1016/j.euromechsol.2014.09.012.

[40] Saboori B, Torabi AR, Ayatollahi MR, Berto F. Experimental verification of two stress-based criteria for mixed mode I/III brittle fracture assessment of U-notched components. Eng Fract Mech 2017;182:229–44. https://doi.org/10.1016/j.engfracmech.2017.06.005.

[41] Hatami F, Ayatollahi MR, Torabi AR. Limit curves for brittle fracture in key-hole notches under mixed mode I/III loading based on stress-based criteria. Eur J Mech A Solids 2021;85:104089. https://doi.org/10.1016/j.euromechsol.2020.104089.

[42] Sih GC, Ho JW. Sharp notch fracture strength characterized by critical energy density. Theor Appl Fract Mech 1991;16(3):179–214. https://doi.org/10.1016/0167-8442(91)90044-K.

[43] Berto F, Ayatollahi M, Campagnolo A. Fracture tests under mixed mode I + III loading: An assessment based on the local energy. Int J Damage Mech 2017;26(6): 881–94. https://doi.org/10.1177/1056789516628318.

[44] Bura E, Seweryn A. The elasto-plastic numerical study of crack initiation in notched PMMA specimens under uniaxial loading conditions – Tension and torsion. Theor Appl Fract Mech 2023;128:104171. https://doi.org/10.1016/j.tafmec.2023.104171.

[45] Derpenski L, Seweryn A. Ductile fracture of EN-AW 2024 aluminum alloy specimens with notches under biaxial loading. Part 1 – Experimental research. Theor Appl Fract Mech 2016;84:192–202. https://doi.org/10.1016/j.tafmec.2016.06.007.

[46] Derpenski L, Seweryn A. Ductile fracture of EN-AW 2024 aluminum alloy specimens with notches under biaxial loading. Part 2 – Numerical research and ductile fracture criterion. Theor Appl Fract Mech 2016;84:203–14. https://doi.org/10.1016/j.tafmec.2016.06.008.

[47] Bura E, Torabi AR, Seweryn A. Fracture prediction in flat PMMA notched specimens under tension - effectiveness of the equivalent material concept and fictitious material concept. Theor Appl Fract Mech 2024;130:104273. https://doi.org/10.1016/j.tafmec.2024.104273.

[48] Torabi AR. Estimation of tensile load-bearing capacity of ductile metallic materials weakened by a V-notch: The equivalent material concept. Mater Sci Engng A 2012;536:249–55. https://doi.org/10.1016/j.msea.2012.01.007.

[49] Torabi AR, Kamyab M. The fictitious material concept. Eng Fract Mech 2019;209:17–31. https://doi.org/10.1016/j.engfracmech.2019.01.022.

[50] Erdogan F, Sih GC. On the Crack Extension in Plates Under Plane Loading and Transverse Shear. J Basic Engng 1963;85(4):519–25. https://doi.org/10.1115/1.3656897.

[51] Novozhilov VV. On a necessary and sufficient criterion for brittle strength. J Appl Math Mech 1969;33(2):201–10. https://doi.org/10.1016/0021-8928(69)90025-2.